ผลของสัณฐานวิทยาของพอลิบิวทิลีนเทเรฟทาเลตต่อสมบัติทางความร้อนและโครงสร้างของฟิล์มพอลิแลคติกเอซิดที่มีรูพรุนในระดับไมโครเมตรโดยเทคนิคการดึงยืดสองทิศทาง

นายชวกร สามทอง

วิทยานิพนธ์นี้เป็นส่วนหนึ่งของการศึกษาตามหลักสูตรปริญญาวิศวกรรมศาสตรดุษฎีบัณฑิต
สาขาวิชาวิศวกรรมเคมี ภาควิชาวิศวกรรมเคมี
คณะวิศวกรรมศาสตร์ จุฬาลงกรณ์มหาวิทยาลัย
ปีการศึกษา 2557

EFFECTS OF MORPHOLOGY OF POLY(BUTYLENE TEREPHTHALATE) ON THERMAL PROPERTIES AND STRUCTURE OF POLY(LACTIC ACID) MICROPOROUS FILMS FABRICATED BY BIAXIAL STRETCHING TECHNIQUE

Mr. Chavakorn Samthong

A Dissertation Submitted in Partial Fulfillment of the Requirements
for the Degree of Doctor of Engineering Program in Chemical Engineering
Department of Chemical Engineering
Faculty of Engineering
Chulalongkorn University
Academic Year 2014

Thesis Title	EFFECTS OF MORPHOLOGY OF POLY(BUTYLENE TEREPHTHALATE) ON THERMAL PROPERTIES AND STRUCTURE OF POLY(LACTIC ACID) MICROPOROUS FILMS FABRICATED BY BIAXIAL STRETCHING TECHNIQUE
By	Mr. Chavakorn Samthong
Field of Study	Chemical Engineering
Thesis Advisor	Associate Professor Anongnat Somwangthanaroj, Ph.D.

Accepted by the Faculty of Engineering, Chulalongkorn University in Partial Fulfillment of the Requirements for the Doctoral Degree

.....Dean of the Faculty of Engineering
(Professor Bundhit Eua-arporn, Ph.D.)

THESIS COMMITTEE

.....Chairman
(Associate Professor Tharathon Mongkhonsi, Ph.D.)

.....Thesis Advisor
(Associate Professor Anongnat Somwangthanaroj, Ph.D.)

.....Examiner
(Associate Professor Siriporn Damrongsakkul, Ph.D.)

.....Examiner
(Associate Professor Seeroong Prichanont, Ph.D.)

.....External Examiner
(Assistant Professor Suttinun Phongtamrug, Ph.D.)

ชวกร สามทอง : ผลของสัณฐานวิทยาของพอลิบิวทิลีนเทเรฟทาเลตต่อสมบัติทางความร้อนและโครงสร้างของฟิล์มพอลิแลคติกเอซิดที่มีรูพรุนในระดับไมโครเมตรโดยเทคนิคการดึงยืดสองทิศทาง (EFFECTS OF MORPHOLOGY OF POLY(BUTYLENE TEREPHTHALATE) ON THERMAL PROPERTIES AND STRUCTURE OF POLY(LACTIC ACID) MICROPOROUS FILMS FABRICATED BY BIAXIAL STRETCHING TECHNIQUE) อ.ที่ปรึกษาวิทยานิพนธ์หลัก: รศ. ดร. อนงค์นาฏ สมหวังธนโรจน์, 106 หน้า.

วัตถุประสงค์ของงานวิจัยนี้คือเพื่อศึกษาผลของสัณฐานวิทยา ประกอบไปด้วยรูปร่างและขนาดของเฟสที่กระจายต่อสมบัติของฟิล์มที่มีรูพรุนระดับไมโครเมตรโดยเทคนิคการดึงยืดสองทิศทาง ฟิล์มที่มีรูพรุนระดับไมโครเมตรถูกเตรียมจากวัสดุเชิงประกอบซึ่งประกอบไปด้วย พอลิแลคติกเอซิด (PLA) เป็นพอลิเมอร์เนื้อพื้นและพอลิบิวทิลีนเทเรฟทาเลต (PBT) เป็นเฟสที่กระจาย วัสดุเชิงประกอบซึ่งประกอบไปด้วยอนุภาคทรงกลมและเส้นใย PBT ที่ขนาดต่างๆ ถูกเตรียมโดยการปรับเปลี่ยนองค์ประกอบเริ่มต้น อุณหภูมิการผสม และระเบียบการผสมของเครื่องผสมระบบปิดและเครื่องวัดสมบัติการไหลแบบคาปิลลารี่

ผลการวิเคราะห์ด้วยกล้องจุลทรรศน์อิเล็กตรอนแบบส่องกราดแสดงให้เห็นว่าเส้นใย PBT สามารถผลิตได้จากการดึงยืดขณะหลอมเหลวและตามด้วยการทำให้เย็นลงอย่างรวดเร็ว การวิเคราะห์สมบัติการไหลยืนยันโครงสร้างแบบโครงร่างตาข่ายแบบสุ่มของเส้นใย PBT มากไปกว่านั้นยังพบว่า PBT เป็นสารก่อผลึกช่วยเร่งอัตราการตกผลึกของ PLA โดยเฉพาะอย่างยิ่งเส้นใยที่มีพื้นที่ผิวจำเพาะมาก ฟิล์มที่ถูกดึงยืดซึ่งประกอบไปด้วยการกระจายตัวของอนุภาคทรงกลมแสดงรูพรุนรูปวงรีในระดับไมโครเมตรอันเนื่องมาจากการหลุดของสายโซ่พอลิเมอร์บริเวณผิวระหว่างเฟส ขนาดอนุภาคทรงกลมของ PBT ส่งผลต่อขนาดรูพรุนแต่ไม่ส่งผลต่อปริมาณรูพรุนของฟิล์มที่ถูกดึงยืด ปริมาณรูพรุนเพิ่มขึ้นอย่างมากถึงประมาณร้อยละ 8 สำหรับฟิล์มที่ถูกดึงยืดที่ประกอบไปด้วยเส้นใยที่กระจายตัวอยู่ ทั้งนี้เนื่องจากการเปลี่ยนรูปเฉพาะตำแหน่งระหว่างเส้นใยที่ประสานกัน ยิ่งไปกว่านั้นฟิล์มที่ถูกดึงยืดมีปริมาณผลึกเพิ่มขึ้นและมีความร้อนแฝงของการตกผลึกเย็นลดลงอันเป็นผลเนื่องมาจากกระบวนการตกผลึกซึ่งถูกเหนี่ยวนำขณะถูกดึงยืด โดยเฉพาะอย่างยิ่งที่อัตราการดึงยืดสูง

ภาควิชา วิศวกรรมเคมี ลายมือชื่อนิสิต .....

สาขาวิชา วิศวกรรมเคมี ลายมือชื่อ อ.ที่ปรึกษาหลัก .....

ปีการศึกษา 2557

5371831521 : MAJOR CHEMICAL ENGINEERING
KEYWORDS: POLY(LACTIC ACID) / POLY(BUTYLENE TEREPHTHALATE) / MORPHOLOGY / MICROPOROUS FILMS / BIAXIAL STRETCHING / ISOTHERMAL CRYSTALLIZATION

CHAVAKORN SAMTHONG: EFFECTS OF MORPHOLOGY OF POLY(BUTYLENE TEREPHTHALATE) ON THERMAL PROPERTIES AND STRUCTURE OF POLY(LACTIC ACID) MICROPOROUS FILMS FABRICATED BY BIAXIAL STRETCHING TECHNIQUE. ADVISOR: ASSOC. PROF. ANONGNAT SOMWANGTHANAROJ, Ph.D., 106 pp.

The aim of this research is to investigate the effects of morphology including shape and size of dispersed phase on the properties of microporous films fabricated by biaxial stretching technique. The microporous films were prepared from the composites containing poly(lactic acid) (PLA) as a polymer matrix and poly(butylene terephthalate) (PBT) as a dispersed phase. The composites containing spherical and fibrous PBT with different particle and fiber sizes were prepared by adjusting initial composition, mixing temperature and mixing protocol of internal batch mixer and capillary rheometer.

Scanning electron microscopic results show that PBT fibers can be produced by melt-stretching and subsequently fast quenching. Rheological characterization confirms the random network structure of PBT fibers. Moreover, it is found that PBT is a nucleating agent accelerating the crystallization rate of PLA, particularly PBT fibers having large specific surface area. The stretched films composed of spherical particles exhibit the ellipsoidal microvoids owing to interfacial debonding of polymer chains. The size of spherical PBT particles affects the void size but not influences the void content of the stretched films. The void content considerably increases to about 8% for the stretched films containing dispersed fiber because of the localized deformation between interdigitated fibers. In addition, the stretched films have increased crystallinity and reduced heat of cold crystallization as a result of strain-induced crystallization, especially at high stretching ratio.

Department: Chemical Engineering Student's Signature .....
Field of Study: Chemical Engineering Advisor's Signature .....
Academic Year: 2014

ACKNOWLEDGEMENTS

First and foremost, I gratefully thank my PhD supervisor, Assoc. Prof. Dr. Anongnat Somwangthanaroj, for motivating me in the scientific journey. She has taken care of me since Master degree project and has continuously provided valuable assistance and advice throughout the PhD program. It is a great honored I was given an opportunity to work with her. I would also like to express my sincere appreciation to Prof. Masayuki Yamaguchi of Department of Materials Science at Japan Advanced Institute of Science and Technology (JAIST). Without their guidance, encouragement and discussion, this research would never have been possible.

I should thank the chairman, Assoc. Prof. Dr. Tharathon Mongkhonsi, and committee members, Assoc. Prof. Dr. Siriporn Damrongsakkul, Assoc. Prof. Dr. Seeroong Prichanont and Assist. Prof. Dr. Suttinun Phongtamrug, for their significant suggestions which are very advantageous for the idea of this research.

I acknowledge the 90th anniversary of Chulalongkorn University fund (Ractchadaphiseksomphot Endowment Fund), and the Royal Golden Jubilee Ph.D. Program (Grant No. PHD/0089/2552) under the Thailand Research Fund (TRF) for the financial support for this research work.

Thanks to all my colleagues in Polymer Engineering Laboratory at Chulalongkorn University and School of Materials Science at JAIST for technical supports over the years. Especially, I am also obliged Mr. Monchai Siriprumpoonthum and Miss Jiraporn Seemork, Ph.D. students of Professor Masayuki Yamaguchi, for their contribute to capillary extrusion and SEM observation.

Finally, I thank almighty my parents from the bottom of my hearth for their endless love and patience since I was born.

CONTENTS

Page

Page

Page

Page

LIST OF TABLES

LIST OF FIGURES

FIGURE Page

FIGURE Page

FIGURE Page

FIGURE Page

FIGURE Page

LIST OF ABBREAVIATIONS

Γ	Interfacial tension
$\dot{\gamma}$	Shear rate
η_d	Viscosity of dispersed phase
η_m	Viscosity of polymer matrix
λ_x	Stretching ratio in x-direction
λ_y	Stretching ratio in y-direction
ν	Poisson ratio
ρ	Density
ϕ	Volume fraction
ω	Angular frequency
σ_{db}	Debonding stress
ΔH_c	Enthalpy of crystallization
ΔH_{cc}	Enthalpy of cold-crystallization
ΔH_m	Enthalpy of melting
ΔH^0_m	Enthalpy of melting for perfect crystalline polymer
Ca	Capillary number
Ca_{crit}	Critical capillary number
d_n	Number-average diameter
d_v	Volume-average diameter

DMA	Dynamic mechanical analysis
DSC	Differential scanning calorimetry
E'	Oscillatory tensile storage modulus
E''	Oscillatory tensile loss modulus
E_Y	Young's modulus
G'	Oscillatory shear storage modulus
G''	Oscillatory shear loss modulus
k	Temperature-dependent crystallization rate constant
MD	Machine direction
n	Avrami index
PBT	Poly(butylene terephthalate)
PD	Polydispersity
PE	Polyethylene
PET	Poly(ethylene terephthalate)
PLA	Poly(lactic acid)
POM	Polarized optical microscopy
PP	Polypropylene
PTFE	Polytetrafluoroethylene
SEM	Scanning electron microscopy
$t_{1/2}$	Crystallization half-time
T_c	Crystallization temperature

T_{cc}	Cold-crystallization temperature
T_m	Melting temperature
TD	transverse direction
TIPS	Thermally induced phase separation
W_a	Work of interfacial adhesion
WVP	Water vapor permeation
X_c	Relative degree of crystallinity

CHAPTER I
INTRODUCTION

1.1 Overview

Microporous polymeric films have received much interest in a broad range of commercial applications including membrane for seawater desalination, breathable surgical bandage, oil absorbing cosmetic wipe and so forth. In the agricultural economics point of view, microporous films are of great important in order to extent the shelf-life and the physical characteristics of the perishable post-harvested fresh produces by allowing the gases and water vapor pass through the films until the gas concentrations inside the packaging reach the equilibrium condition. Namely, the post-harvested fresh produces respires slowly and imitates the hibernation state.

Several well-known techniques have been developed to produce the microporous films with high porosity; however, they involve a use of organic solvent and a contamination of hazardous solvent and cost of waste solvent treatment are the major disadvantages to be used as food packaging. Therefore, mechanical stretching of the homopolymers (*i.e.*, isotactic polypropylene) and the polymer composites in the solid state is an important method to fabricate the microporous films. Nonetheless, concerning over the perspectives of view of global environmental impact, poly(lactic acid) (PLA), which is currently one of the most promising linear

aliphatic polyesters, is chosen owing to its high strength, high modulus, transparency, biodegradability, and biocompatibility. The major shortcomings of PLA, however, are brittleness, poor melt strength, low gas permeation, and, in particular, intrinsic slow crystallization rate compared with those of semicrystalline polyolefin, leading to poor processability under supercooling condition. Moreover, stretching single PLA sheets is difficult to yield the desired properties of the microporous films, thus the PLA composites with the addition of secondary polymer constituent is conducted in this work to improve the properties of PLA and to fabricate microporous film.

It has been reported that the morphology dominantly influences the properties of the composites. For instance, the composites containing spherical particles usually have high impact resistance, while the composites containing fibrous dispersion gives excellent unidirectional mechanical strength. Unfortunately, most researchers reluctantly investigated the effect of shape of dispersed particle on the properties of the composites from wholly different particle types. Herein, the methodology to produce both spherical and fibrous dispersions from a single pair of binary polymer composites is introduced.

The aim of this dissertation is to examine the effects of size and shape, *i.e.*, sphere and fiber, of poly(butylene terephthalate) (PBT) dispersed phase in PLA matrix on the properties of the composites and the porous structure of the biaxially stretched films. The PLA/PBT microporous films are prepared by biaxial stretching machine in

two different stretching modes including planar deformation and equibiaxial deformation. Furthermore, the relation between structural feature and isothermal crystallization kinetics and morphology of the PLA/PBT composites is examined by using a theoretical kinetic Avrami model.

1.2 Objectives of the research

1. To propose the methodology to achieve the spherical dispersion and fibrous dispersion of PBT in the PLA composites having the same final composition.

2. To examine the effects of shape (*i.e.*, sphere and fiber) and size (*i.e.*, small. medium, large) of PBT on the rheological, thermal and dynamic mechanical properties as well as porous structure and void content of the PLA/PBT unstretched and stretched films.

3. To comparatively study the properties of biaxially stretched films produced by two different techniques, *i.e.*, planar deformation and equibiaxial deformation.

4. To evaluate the isothermal crystallization kinetics and morphology of the PLA/PBT composites by using a theoretical kinetic Avrami model

1.3 Scopes of the research

1. The spherical and fibrous dispersions of PBT having three different sizes are mainly obtained by an internal batch mixer and a capillary rheometer. The morphology of prepared composites is observed by scanning electron microscope and optical microscope.

2. The PLA/PBT sheets are stretched by two distinct modes, *i.e.*, planar deformation and equibiaxial deformation. The stretching ratio also is also varied. The void content, thermal properties and water vapor permeation of the stretched films are also measured.

3. The isothermal crystallization kinetics and morphology are studied at isothermal temperature, ranged from 115-130 ^{o}C, by differential scanning calorimetry (DSC) and polarized optical microscopy (POM).

1.4 Organization of the research

To clarify the descriptions of this work, the dissertation is categorized into several chapters as follows.

The background in Chapter II consists of the comprehensive research methodology covering fundamental theory, and the idea of how to reach the targets by using knowledge of polymer engineering and science. The description begins with

the importance of microporous films as an agricultural packaging for export of the perishable fresh produces as well as the metabolism of post-harvested fresh produces. Subsequent topic is the techniques to prepare microporous materials, especially the solventless mechanical stretching of polymer composites. The advantages and disadvantages of plain PLA as well as the improvement of properties of PLA by incorporation of second phase, forming the composites, are also stated.

Chapter III is devoted to the literature reviews of this dissertation, including effects of morphology of the composites, interfacial modification of particle, size of particle, and stretching mode on the properties and porous structure of the composites and stretched films.

In Chapter IV the methodology to achieve the composites containing three differences in size (small, medium and large) and shape (sphere and fiber) at the same final composition is proposed. Further, the investigation of the effect of size of spherical and fibrous dispersions of PBT dispersed domains on the rheological, thermal and dynamic mechanical properties of PLA composites is given. Eventually, the porous structure, thermal properties, and water vapor permeation of the microporous films prepared by biaxial stretching of the PLA/PBT composites are introduced. The stretching modes include planar deformation and equibiaxial deformation.

In Chapter V the studies concerning the effects of shape and size of PBT on the isothermal crystallization behavior of the PLA/PBT composites by DSC are presented. The theoretical Avrami model is conducted to explain the isothermal crystallization kinetics. Moreover, the isothermal crystallization morphology is also monitored by POM to examine the development of crystalline structure of PLA.

Chapter VI contains the overall conclusions of this dissertation. Recommendations are also listed for the future works.

CHAPTER II
BACKGROUND

2.1 Post-harvested fresh produces

2.1.1 Problem of export of post-harvested fresh produces

Thailand has a tropical climate suitable for the agricultural activities to harvest a large variety and high quality fresh produces, *i.e.*, fruits, vegetables, and flowers, for not only Thai people, but also other foreign countries. In 2013, Thailand earned proximate 1,300 million U.S. dollar from exportation of these fresh produces and this income tends to continuously grow in the future [1]. However, Department of International Trade Promotion, Ministry of Commence reported that about 15-30% of total value was lost during overseas transportation because the transportation time by sea cargo is too long and the physical characteristics of the perishable post-harvested fresh produces have already been changed before reaching the market. To solve the problem, it is of great importance to understand what happened to these fresh produces after post-harvest.

2.1.2 Metabolism of post-harvested fresh produces

Before harvest, fruits and vegetables generally consume nutrient and water from the soil and carbon dioxide in the air and release oxygen in the presence of light for respiration via photosynthetic reaction. On contrary, the post-harvested fresh produces are still living and perform their metabolism activities such as ripening, aging and decay, in which they consume oxygen and release water vapor, carbon dioxide and sometimes ethylene, leading to great changes in sensory qualities such as appearance, texture, color, flavor, and aroma. The storage conditions, such as temperature and humidity, are also crucial to reduce their metabolism; however, the concentrations of these gases in the packaging need to be controlled either. For example, the immature bananas can change into mature ones very fast if ethylene concentration is too high because it is a ripening hormone, stimulating the production of enzymes in the cells' tissues leading to accelerated ripening process.

2.1.3 The importance of modified food packaging

When the airtight plastics are used as food packagings, the accumulation of these gases and water vapor results in several post-harvest defects like carbon dioxide injury, growth of fungi/mold and over-ripening. Further, the post-harvested fresh produces cannot breathe anymore after a long period of time because the oxygen inside is depleted. The principle of modified food packaging is imitating the post-

harvested fresh produces in the hibernation state and one of the options is a replacement of the gas inside by a desired gas mixture like inert gases, *i.e.*, nitrogen, carbon monoxide, and carbon dioxide, in order to minimize the oxygen content as low as possible. Thus, post-harvested fresh produces respire slower and, certainly, generates a smaller amount of ripening-promoted ethylene gas. This preservation technique is called *modified atmosphere packaging* (*MAP*) [2-4]. Nevertheless, MAP technique is complicated since the suitable fed gas mixture need to be known, which always varied depending on the type of each fresh produce.

The alternative route is using the packaging that allows the gas molecules permeate through the polymeric films. The difference in gas concentration inside and outside the packaging is the driving force. At first, the post-harvested fresh produces consume oxygen in the normal rate; however, their respiration rate is slower because of lower oxygen concentration. In conclusion, microporous polymeric films are important for agricultural industries in order to maintain the physical characteristics and prolong the shelf-life of perishable fresh produces by allowing gas and water vapor to pass through the voids of the films until reaching the equilibrium condition, at which the fresh produces are in the hibernation state.

2.2 Development of microporous materials

2.2.1 Definition of microporous materials

Porous materials have been intensively prepared in a broad range of applications including membranes for seawater desalination and gas separation, agricultural packaging, and biomedical engineering such as breathable bandage and scaffold. The performance of porous materials strongly depends on pore size and pore size distribution. According to IUPAC recommendations for the characterization of porous solids, porous materials can be categorized by size into 3 groups: micropores ($d < 2$ nm), mesopores ($2 \text{ nm} < d < 50$ nm) and macropores ($d > 50$ nm) [5]. However, the term “micropores” is covered “mesopores” and “macropores” as well in the membrane industries. In case of cylindrical shape and slit-like shape, pore size is measured from diameter and width, respectively.

2.2.2 Fabrication of microporous films with using solvent

There are numerous methods for preparation of microporous materials having distinct advantages and disadvantages, which are explained as follows. Sidney Loeb and Srinivasa Surirajan introduced the first anisotropic reverse osmosis membrane from cellulose acetate in 1963 by using dry-wet technique (Loeb-Sourirajan technique) [6]. The theory of this technique is a precipitation of polymer solution casted onto a glass

plate by partial solvent evaporation and immersion in non-solvent (such as water) forming a membrane [7]. The parameters affecting microstructure include concentration of polymer solution, solvent type, solvent evaporation period, and relative humidity [8,9].

Another wet technique is thermally induced phase separation (TIPS) process which involves phase inversion of solid-liquid phase by a decrease of temperature, removing thermal energy from the system. The polymer is dissolved in a diluent, which behaves like solvent at high temperature, then casted onto glass plate. The temperature of polymer solution decreases; therefore, the solubility of a diluent also decreases at a suitable point, where phase separation occurs. Finally, a diluent is washed out with solvent, which acts as a non-solvent for polymer [10,11].

Selective solvent extraction (sometimes called template leaching) is one of the easiest ways to prepare symmetric microporous materials. The polymer is blended with extractable materials (porogen phase) through melt processing to form heterogeneous films. After that, a solvent, which is a non-solvent for main polymer matrix, is used to extract a porogen phase and the microporous films are achieved. The extractable materials can possibly be low-molecular weight compounds, such as starch [12], or polymeric materials, such as polystyrene [13].

Even though these wet techniques have been applied commercially in membrane industries and the prepared membranes have high porosity, the crucial disadvantages are a production of a large amount of waste solvents and cost of waste solvent treatment. Also, a contamination of hazardous solvent is a high risk for applying microporous films as food packaging. Furthermore, it is inconvenient to deal with thermoplastic polyolefin, *i.e.*, polyethylene (PE) and polypropylene (PP), because these polymers are very difficult to dissolve in common organic solvents at room temperature.

2.2.3 Fabrication of microporous films without using solvent

These dry techniques are specifically advantageous because of no solvents involved. The non-porous films can be simply created numerous holes by piercing the films with laser beam [14,15]. This perforation generates systematic distribution and controllable size of holes by adjusting the pulse energy and pulse number; however, this process is quite expensive regarding the prices of laser source, beam splitter and other instrumental components. Although the “hole-maker” instrument can be replaced by sharp needle instead of laser beam, the pore size is generally not in the microscopic level and the problem for packing post-harvested fresh produces such as an attack from a growth of bacteria and fungi is possibly found.

Henceforth, mechanical film stretching is introduced for microporous film fabrication since it is an important polymer processing to generate film-like food packaging in the real industries. Technically, the precursor sheets are extruded from the die and subsequently stretched in machine direction (MD) and transverse direction (TD), as shown in Figure 2.1, at room or elevated temperature to obtain the desired film thickness and polymer chain orientation. Also, this mechanical film stretching has been conducted to create commercial microporous films as detailed in the next section.

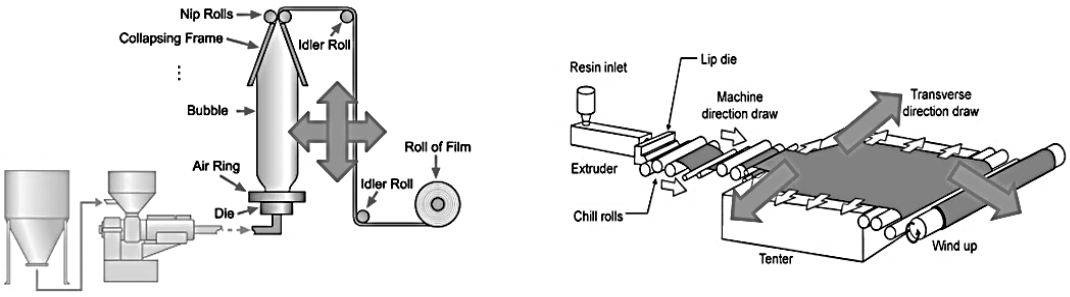

Blown film extrusion Cast film extrusion with biaxial stretcher

Figure 2.1 Mechanical film stretching in the industrial polymer processing

2.2.4 Fabrication of microporous films by mechanical stretching of homopolymer

The alternative routes to obtain microporous films include stretching homopolymer sheets. It has been developed extensively from polyethylene (PE) and

polypropylene (PP) by Celanese Corporation in a registered trademark of Celgard® for medical applications such as a breathable bandage [16], and battery separators [17]. Also, W. L. Gore and Associates invented waterproof porous fabric made from expanded polytetrafluoroethylene (PTFE) [18]. The mechanism of microstructure development of these commercial films (Figure 2.2) during the film stretching is detailed below.

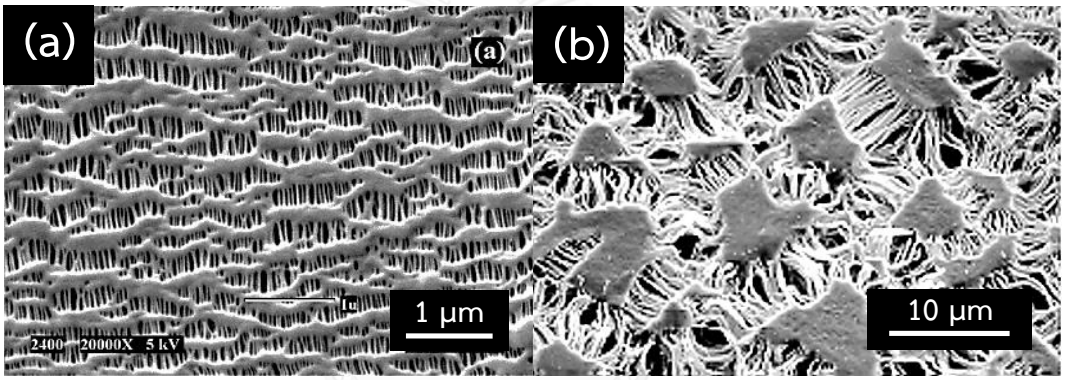

Figure 2.2 SEM images of (a) the surface of single layer Celgard® 2400 (PP) [16]; (b) Gore-Tex® membrane (size of island is about 10 µm) [18]

Semicrystalline polymer (PE and PP) contains two different polymer chain orientations in solid state: amorphous and crystalline. Amorphous region is where the polymer chains align randomly and irregularly. On contrary, crystalline region is where polymer chains can pack together orderly usually in the same direction as crystal growth and external stretching. If the polymer chains are folded in a stack form, it is called *lamellar*. In semicrystalline polymer, the crystalline lamellar is stacked together

with the amorphous region in between or surrounds, and are connected by polymer chains. In case the crystalline polymer chains do not only fold in a lamellar structure, but grow in three-dimensional direction similar to branches sharing the same origin, it is known as *spherulite*. The morphologies of lamellar and spherulite are shown in Figure 2.3.

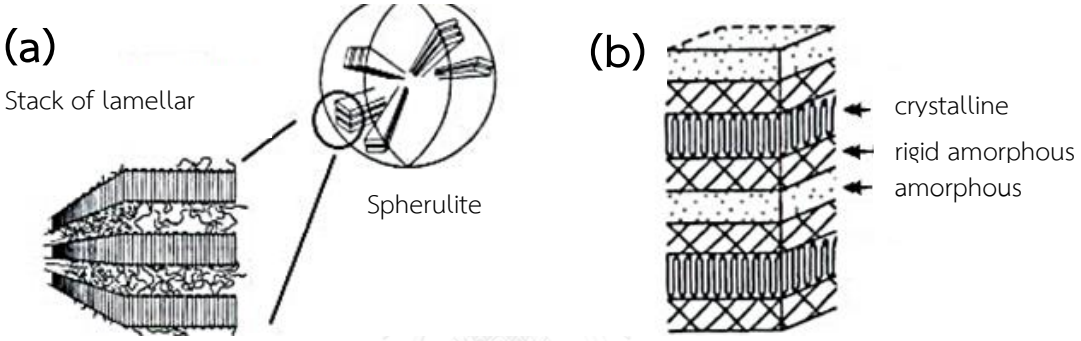

Figure 2.3 (a) Morphologies of lamellar and spherulite; (b) the three-model of semicrystalline polymer [19]

The key for preparing porous film from single semicrystalline polymer is that the precursor films with a row-nucleated lamellar morphology is prepared first by cooling the molten films, followed by annealing and then applying external stress at low temperature (room temperature) for producing microvoids as a result of lamellar spreading and, in turn, at high temperature for expanding and stabilizing the pores [20,21]. The purpose of annealing is not only to thicken the lamellae size (which

generally in an order of 10 nm thick), but also to eliminate the defects in crystalline region. The lamellar spreading is presented in Figure 2.4.

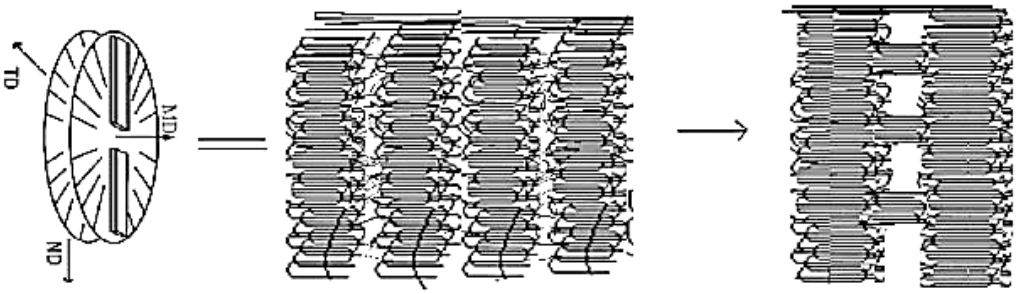

Figure 2.4 Schematic diagram of lamellar spreading of a row-nucleated lamellar structure in machine direction (MD) [20]

In some cases, lamellar spreading may not be the only mechanism causing the creation of porous structure from single polymer. The microporous isotactic PP films with porosity of 30-40%, average pore size of 0.05 μm and narrow pore size distribution were prepared by biaxial stretching of PP non-porous film having high β-crystal content [22]. The microvoids were formed because of the volume contraction resulted from β-to-α crystalline transformation as confirmed by XRD data [23]. Nonetheless, both lamellar spreading and β-to-α crystalline transformation limited the average pore size of porous film due to the crystalline domain of semicrystalline polymer [24]. Consequently, many works have also attempted to prepare porous films by mechanical stretching of semicrystalline polymer added filler and immiscible polymer blends in order to obtain a porous film with smaller pore size and higher porosity.

2.2.5 Fabrication of microporous films by mechanical stretching of multiphase polymeric materials

Apart from mechanical stretching of homopolymer sheet, the prepared sheets can be the multiphase polymeric systems including polymer blends and polymer composites because the lamellar morphology is unable to achieve in some polymers owing to the unique stereoregularity, affecting polymer chain folding behavior under cooling condition. This is the reason why the porous materials are generated from isotactic PP only, but not from atactic or syndiotactic PP. Moreover, mixing polymer with other polymer constituents or inorganic particles is an effective approach widely used in order to improve the properties of finishing product by combining their advantageous properties in the single system.

The idea for making microporous film from these multiphase polymeric materials is based on the fact that the microvoids originate at the polymers' interface if the given force via mechanical stretching overcomes the interfacial interaction between two polymer phases. This phenomenon is called *debonding*. The preparation begins with producing the precursor films from polymer blends first (it can be fiber and hollow fiber in some cases [25]), for example, by twin screw extruder equipped with a flat sheet die, following by film stretching in uniaxial or biaxial directions under controlled deformation and temperature. This strategy is also known as *post-extrusion*

film stretching process and it is most likely similar to the lamellar separation, *i.e.*, the microvoids have to be achieved first upon film stretching at low temperature and, consecutively, they are stabilized at elevated temperature.

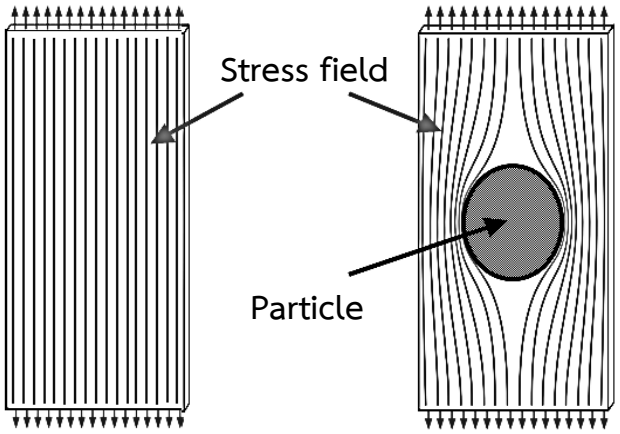

Figure 2.5 Stress distribution in the films upon stretching

2.3 Biodegradable polymer composites

The choice of material for microporous films sometimes depends on the final applications. For instance, polyolefins are used because they have high corrosion resistance, which is suitable for membrane separation. In this work, we have focused on producing microporous films by mechanical stretching of the composites comprising biodegradable polymer.

2.3.1 Advantages and disadvantages of neat PLA

Concerning over the perspectives of view of global environmental impact and waste management, biodegradable biopolymers have been recently attracted great interests both in industry and academia to substitute the traditional petroleum-based thermoplastics since they can be derived from annually abundant renewable resources like corn and starch without being influenced by the oil prices and can completely decompose via hydrolysis in soil into carbon dioxide and biomass in a relative short time under the suitable conditions [26,27]. Poly(lactic acid) (PLA), which is currently one of the most promising linear aliphatic polyesters, has been intensively used in a broad range of applications, *i.e.*, scaffold for bone tissue engineering [28,29] and environmentally-friendly agricultural packaging [30-32], owing to its high strength, high modulus, transparency, biodegradability, and biocompatibility. The major shortcomings of PLA, however, are brittleness, poor melt strength, and, in particular, intrinsic slow crystallization rate compared with those of semicrystalline polyolefin, leading to poor processability under supercooling condition [33]. Therefore, controlling the crystallization rate of PLA from the molten state, so-called melt crystallization, is a crucial factor for not only shortening the practical processing cycles, but also achieving good optical appearance as well as satisfactory thermal and mechanical characteristics of the end-use products.

2.3.2 Role of morphology on the properties of the composites

The properties of PLA are enhanced by incorporation of second phase, which can possibly be inorganic rigid particles, naturally available fibers, electrically conductive fillers and other polymers. The morphology of polymer composites is demonstrated in Figure 2.6.

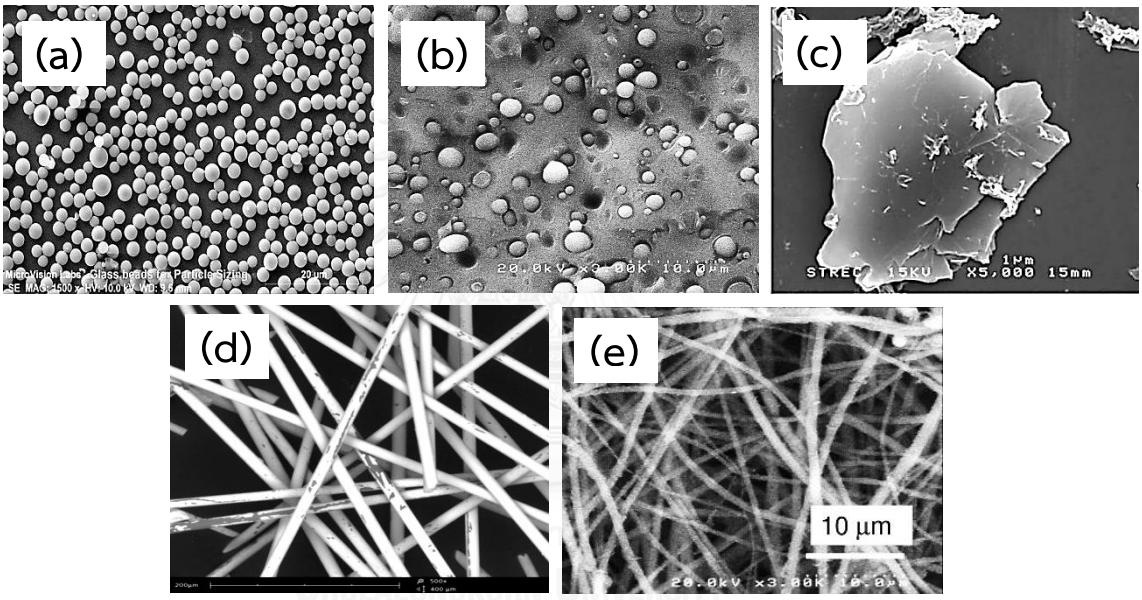

Figure 2.6 Morphology of particle in composites: (a) rigid sphere (glass bead), (b) polymeric sphere (polystyrene phase in polypropylene matrix), (c) plate (graphene), (d) rigid fiber (glass fiber), and (e) polymeric fiber (melt-stretched poly(butylene terephthalate))

For instance, natural rubber increases elongation and toughness significantly because the crosslinked network absorbs and distributes the internal stress [34]. The

PLA nanocomposites containing graphene nanoplatelets showed excellent thermal and electrical conductivity [35]. Moreover, the crystallization rate of PLA prominently accelerated with the presence of inorganic fillers, *i.e.*, titanium dioxide [36], organoclay [37] and talc, and other polymeric constituents, *i.e.*, poly(ethylene terephthalate) (PET) [38], poly(butylene succinate) (PBS) [39], poly(butylene adipate-*co*-terephthalate) (PBAT) [40]. Moreover, PLA composites containing polytetrafluoroethylene (PTFE) and poly(butylene terephthalate) (PBT) nanofibers showed the pronounced strain-hardening behavior in elongational viscosity [41-44].

Considering only the shape of dispersed phase, the composites containing spherical particles usually have high impact resistance. The sheet-like particles have the barrier properties to prevent the gas permeation of the samples. The fibers one-directionally aligned in the samples can increase the unidirectional mechanical strength, whereas the network structure of fibers improves the melt strength of the molten polymer [45]. Consequently, the morphology of the composites is a crucial parameter affecting the final properties of the end-use products. However, it is practically difficult to achieve these morphologies from a single pair of polymer system. In this dissertation, the methodology to prepare spherical and fibrous dispersion from a pair of binary polymer composites is suggested.

CHAPTER III

LITERATURE REVIEWS

3.1 Effect of morphology on the properties of stretched films

In the binary immiscible polymer blends containing low concentration of minor component, the blends contain the dispersed spherical domains distributed in matrix as a result of high interfacial tension, as displayed in Figure 3.1.

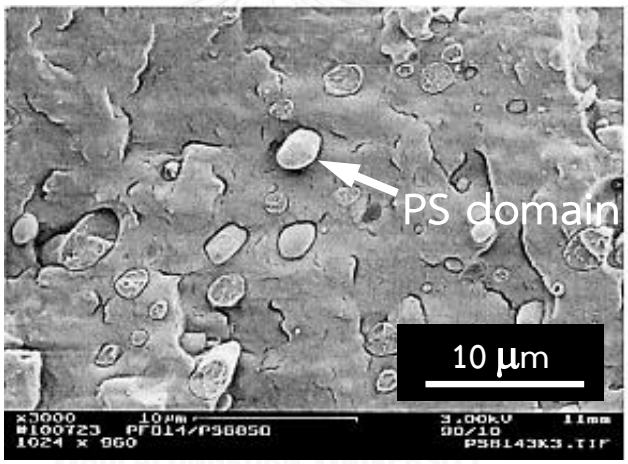

Figure 3.1 SEM micrograph of fractured surface of PP/PS blends [46]

Chandavasu et al. [24,46,47] prepared PP microporous films from the immiscible blends containing spherical dispersion of polystyrene (PS) and poly(ethylene terephthalate) (PET) with pore size in a range of 2 to 50 nm using melt processing and post-extrusion film stretching treatment. The precursor films were uniaxially and biaxially drawn (100-500% with respect to initial dimension) at

temperature below glass transition temperature (T_g) of minor phase following by subsequently stretching at elevated temperature to stabilize the porous structure. In addition, they also analyzed the stress distribution in PP/PS (90/10) blends under deformation using finite element analysis in solid state as displayed in Figure 3.2 and found that the stress concentration of bulk near the minor phase domain increased 1.2-1.5 times that of stress applied, indicating that the minor domain phase (PS or PET) acts as stress concentrator. The interfacial adhesion between two immiscible polymer blends in precursor film was relatively weak due to high interfacial tension, thus if the stress overwhelms an interfacial adhesion, the minor phase domains are debonded and the microcracks are initiated and propagated into a major phase via crazing mechanism. The PP/PS (90/10) microporous films showed an average pore diameter of 10.1 nm and surface porosity of 11.1 %, as illustrated in Figure 3.3.

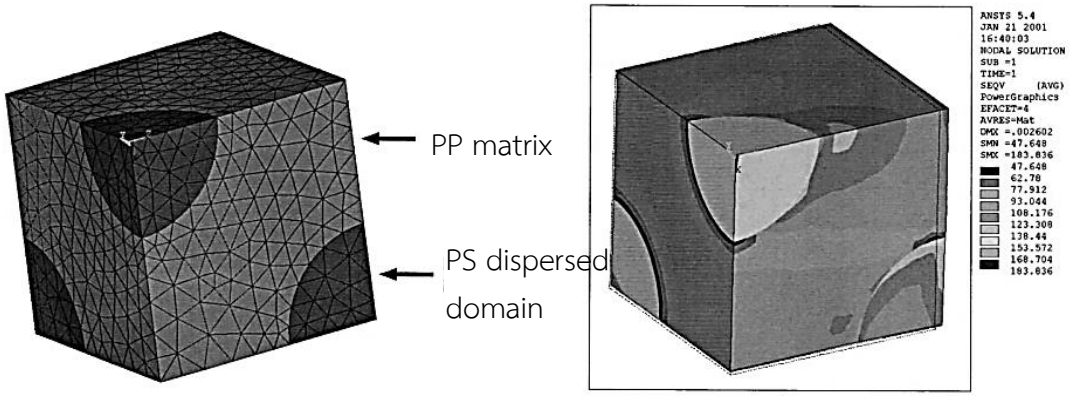

Figure 3.2 Finite element analysis of PP/PS (90/10) blends to calculate the stress distribution in the regions near the dispersed phase domains [46]

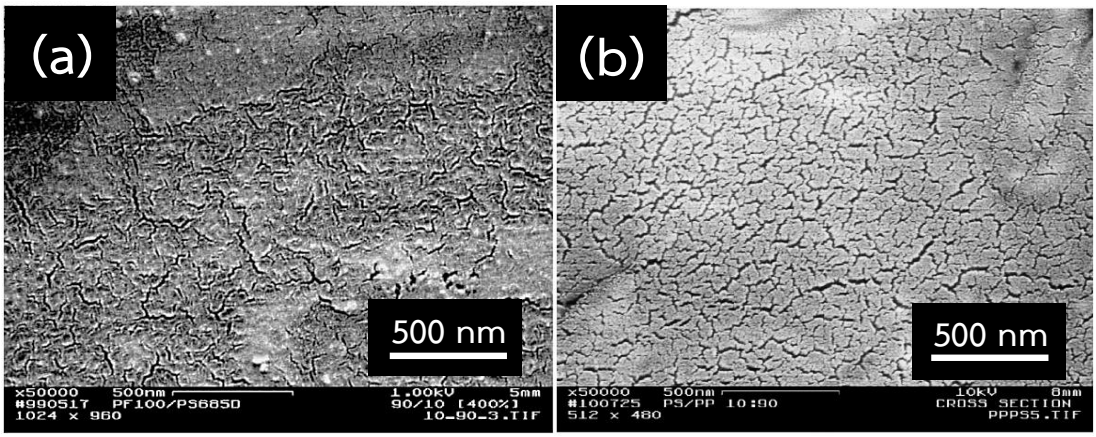

Figure 3.3 SEM micrographs of microporous PP/PS (90/10) film upon uniaxially stretching by 400%: (a) surface; (b) cross-section [46]

Stretching of the composites containing spherical particles gave the similar trend. The γ-alumina filled high density PE precursor films prepared through extrusion were uniaxially drawn to 600% of original length in a bath containing propylene glycerol to yield porous films with 45.3% porosity and approximate average pore size of 0.48 μm at stretching temperature of 80 ^{o}C [48]. Further, the biaxially stretched films of PP and HDPE filled with 15 wt% of $CaCO_3$ particles showed the non-interconnected porous structure, generated from the particle-matrix decohesion owing to weak interfacial specific interaction between polymer and particles [49].

When the concentration of minor component increases and reaches the percolation threshold, the dispersed phase transforms into matrix and the system has co-continuous morphology. The co-continuous PE/PC (50/50) microporous films having uniformly pore size in a range of 40 to 200 nm (average pore size of 100 nm) were

generated upon post-extrusion film stretching [13]. The porosity in this work was not displayed but it was found that oxygen permeation of PE/PC (50/50) films uniaxially stretched at 125% (MD) was 2 times that of non-stretched ones.

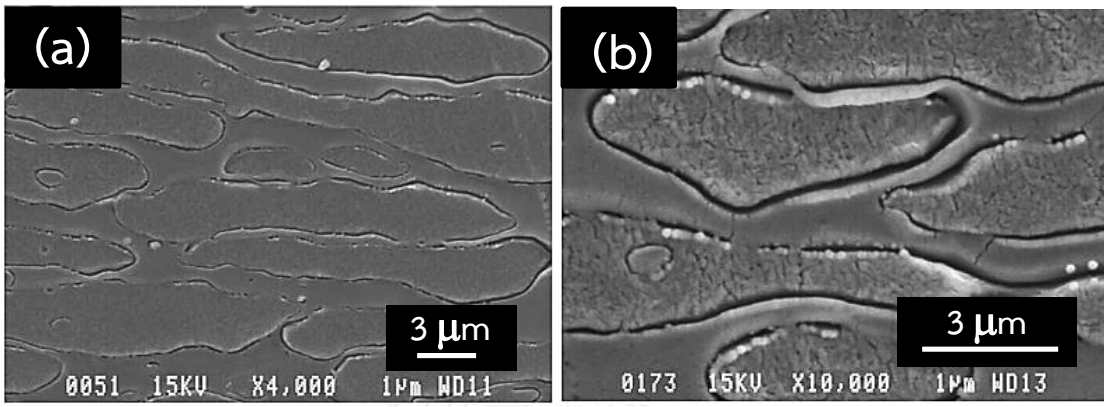

Figure 3.4 SEM micrographs of cross-sectional fractured surface of PE/PC(50/50); (a) non-stretched and (b) stretched at 165% in MD and 70% in TD [13]

Most studies have focused only on preparing microporous films from the polymer composites or polymer blends containing dispersed spherical phase; however, a dispersion of nanofiber in the composites is an interesting candidate owing to the availability of nanofiber nowadays since several methods to prepare nanofiber are proposed. The methodology to generate *in situ* fibrillar structure in the polymeric composites by manipulating the manufacturing conditions of polymer processing equipment is an interesting choice that has been comprehensively proposed. For instance, based on a concept of microfibrillar composites technology Shields et al. [50]

prepared composites of PET microfibrils embedded in a continuous polyethylene matrix by extrusion following by cold-drawing. Moreover, Yamaguchi and coworkers [43,44] created the fibrous dispersion of flexible fine poly(tetrafluoroethylene) (PTFE) and poly(butylene terephthalate) (PBT) in PLA matrix by capillary extrusion and subsequent melt-stretching. Melt-stretching of polymer blends in molten state at a high level of shear forces results in a deformation of the dispersed spheres into fibers. In addition, rapid quenching after extrusion leads to a stable fibrous dispersion system and hinders the deformation of dispersed polymer component into spherical droplets again as a result of high interfacial tension [51,52]. Additionally, it should be noting that this technique needs three key requirements: (1) the constituent polymer must have high drawability to produce fibrillar structure, (2) both polymer must be able to be melt-processed at single temperature without the thermal degradation, and (3) the dispersed polymer must have melting temperature exceeding that of polymer matrix by a least 40 ^{o}C. Therefore, a pair of binary polymers for fibrillation is limited.

There have been a lot of researches on investigating the polymer composites containing fibrous dispersion [41-44,53-57]. Incorporation of poly(butylene succinate) (PBS) nanofibers in poly(lactic acid) (PLA) matrix prepared by melt-stretching using a capillary rheometer can enhance the modulus, degree of crystallinity and cold-crystallization behavior in comparison with those containing spherical PBS [57]. Ali et al. [41,42] found that polytetrafluoroethylene (PTFE) flexible nanofibers in continuous

PP phase drastically improved the drawdown force and primary normal stress difference of the blends. Further, Yamaguchi and coworkers [44,58] found that PLA composites composed of a small amount of fibrous PBT in solid state showed the marked strain-hardening behavior in uniaxial elongational viscosity because of flexibility and interdigitation of the PBT nanofibers (Figure 3.5). Although incorporating the glass fiber with large aspect ratio in gave the increased steady-state elongational viscosity, the composites did not show the strain-hardening behavior in elongation viscosity [59]. This result implies that the flexibility also plays a key role in the rheological properties of the composites.

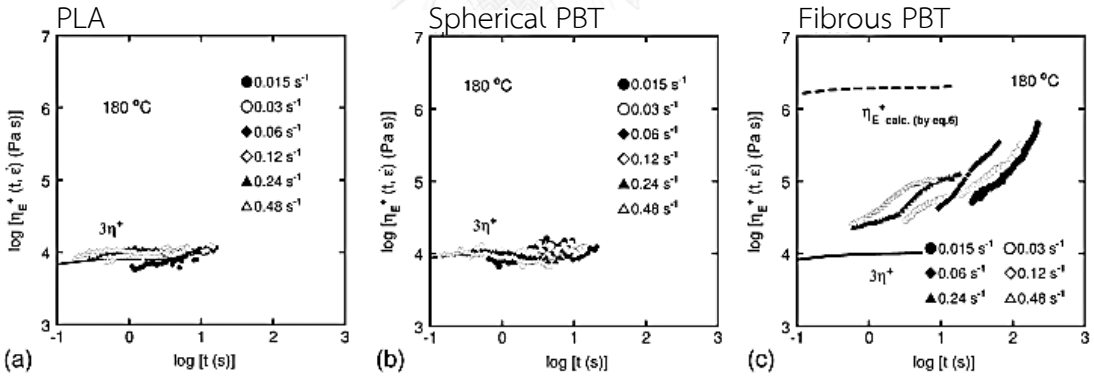

Figure 3.5 Growth curves of uniaxial elongation viscosity at 180 °C for PLA and its composites containing 1 wt% of spherical and fibrous PBT dispersion [44]

Up to now, however, few authors have specifically addressed the void formation in polymer composites with rigid fibers considering the classical fracture mechanics [60-62]. The initiation of microvoids and their propagation were typically

observed around the ends of glass fiber, where the highest shear stress is located, in polyester composites because of weak bonding due to no surface modification of fiber [62]. The formation of microvoids usually occurs along with the stress-whitening, as seen in the glass fiber reinforced polyester composites during tensile tests [60]. It was also mentioned that the stress concentration increases with increasing aspect ratio of the dispersed phase [63]. Nevertheless, the main purpose of their works is to clarify the failure mechanism of rigid fiber-reinforced composites, not to create porous materials. To the best of our knowledge, however, combining the advantages of nanofiber dispersion and applying the fundamental knowledge of fracture mechanism to prepare microporous films have not been well achieved yet.

3.2 Effect of interfacial modification on the properties of stretched films

The polymer blends can be miscible or immiscible; that is, the polymer chains of each phase entangle or dissolve into another phase when their stereoregularities and polarities are similar, resulting in the miscible blends with thick interfacial thickness and strong interfacial adhesion. However, most multicomponent polymer systems usually form immiscible blends and the mechanical properties are also low because of poor interfacial strength. Therefore, some surface modification techniques, such as surface treatment of particles and addition of compatibilizer, have been conducted. Lepers and coworkers [64] investigated the effect of (styrene-ethylene-butadiene-

styrene)-*graft*-maleic anhydride (SEBS-*g*-MA) copolymer on the porous structure of biaxially stretched PET/iPP blends. Although Young's modulus and stress at break increased, they found that the void volume in the sample dropped from 60% to almost zero at a minute amount of additional SEBS-*g*-MA, as shown in Figure 3.6. This result can be explained by the fact that the interfacial strength between PET and iPP phases increased drastically and the stress upon film stretching could not overcome this improved strength. The same trend was also mentioned by Wu [65] who studied the effect of compatibilizer on porous structure of uniaxially stretched PP/PS blends. Namely, the compatibilizer reduced the size of dispersed phase domain and enhanced interfacial adhesion, causing the microvoids with much smaller length. In summary, the production of porous materials is pronounced for immiscible blends or the interfacial strength between polymer matrix and inorganic fillers is poor.

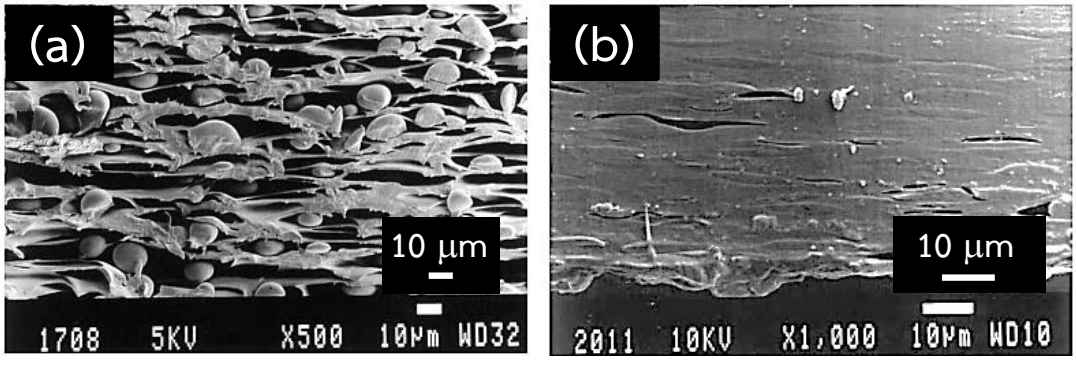

Figure 3.6 Morphology of the stretched blends: (a) PP/PET(20:80) non-compatibilized, and (b) PP/PET(20:80) with 10% SEBS-*g*-MA in the PP [64]

3.3 Effect of particle size on the properties of the stretched films

The smaller the particle becomes, the higher the specific surface area they have. This is a very important reason nanocomposites have been attracted great attention in a last few decades. The nanocomposites showed the considerable improvement of mechanical strength in comparison with composites containing micron-size particles [66-69]. In terms of thermal properties, it was found that the crystallization rate strongly depends on the surface area of the dispersed phase since it is the nucleation site for polymer matrix to orderly fold, forming crystalline structure. For instance, Wang et al. [70] said that the surface topography (level of roughness) rather than surface chemistry is a dominant effect for nucleation process during isothermal crystallization in PLA/sisal fiber composites since rough surface of treated fiber has larger nucleation sites. However, Kose and Kondo [71] reported that not only the size effect, but also degree of dispersion of cellulose nanofibers are the major factors for the crystallization behavior of PLA.

In the mechanical point of view, the particle acts as stress concentrators, accumulating the internal stress around their surfaces higher than those in the matrix phase upon loading. More importantly, the degree of stress concentration is more intense in case the particle becomes larger. On the other words, the stretched films composed of large particle should give higher porosity. Nevertheless, Wu et al. [72] showed that the air flow of PE/$CaCO_3$ stretched films gradually increased as a function

of particle size and then reached an optimum value at average particle diameter of 0.7 micron (Figure 3.7), which can be explained by the fact that the particles were hardly well dispersed and tended to agglomerate and, therefore the surface area of the particles as an origin of void opening process was also reduced.

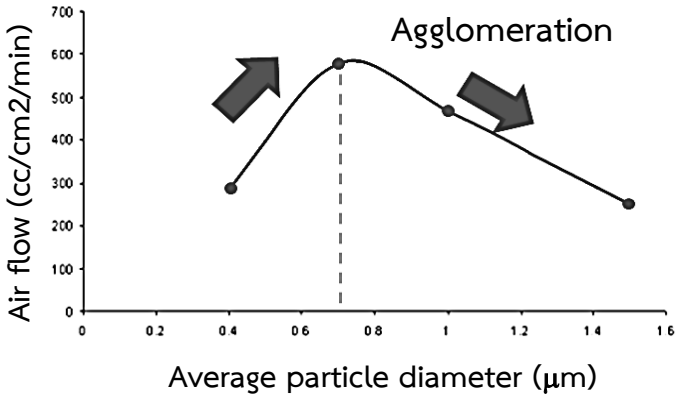

Figure 3.7 Effect of mean particle size on breathability of PE/$CaCO_3$ composites [72]

3.4 Effect of stretching mode on the properties of the stretched films

The flow or deformation in the field of material science can be extensional such as in film stretching, or shear such as in cone-plate rheological measurement. The examples of extensional stretching modes are shown in Figure 3.8. During uniaxial deformation, the samples are purposely deformed in one direction (for example x_1) by mechanical stretching while the sizes in other two directions reduce. The melt-spinning in fiber forming production is a very clear exemplary industrial polymer processing. In contrast, the stretching is called planar deformation in case the samples are stretched

in x_1 direction with a resultant decrease in size in x_2 direction while the size in x_3 direction is kept constant throughout the whole deformation. Finally, biaxial deformation is when the stretching is performed in two directions simultaneously.

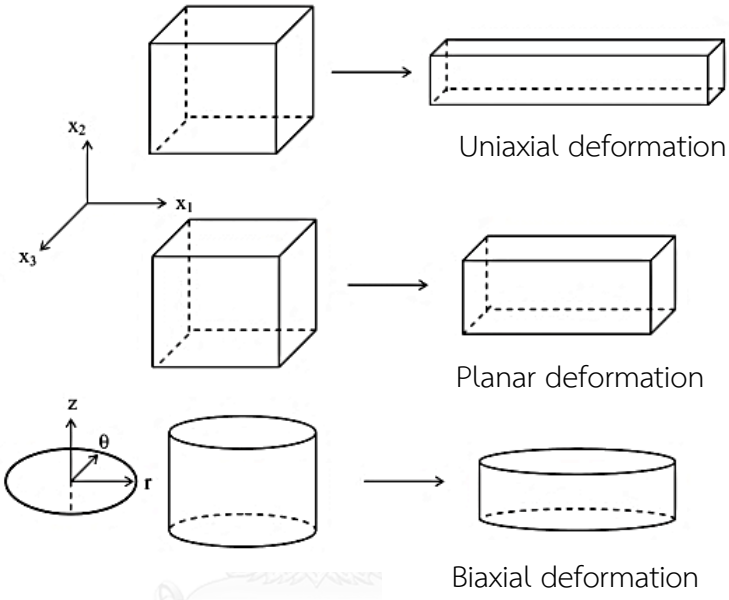

Figure 3.8 Uniaxial, planar and biaxial deformation [73]

In the industrial film processing, the sheets were extruded from the flat sheet die of extruder and subsequently stretched in different conditions, *i.e.*, stretching rate, stretching ratio, sequence of stretching direction, and temperature, primarily in order to obtain the orientation of polymer chains and, in turn, to improve mechanical properties of the stretched films. Ou and Cakmak [74,75] investigated the structural evolution of PLA biaxially stretched films in rubbery state by planar and biaxial deformation. They found that the orientation of PLA chains was prominently enhanced

and biaxial deformation gave poor crystalline order compared with planar deformation as evidenced by the results of birefringence, thermal analysis and WAXD. An enhancement of crystalline structure is a result of strain-induced molecular orientation in the film stretching direction [76,77]. Furthermore, Zhang et al. [78] mentioned that the crystallinity and orientation of PLA improved with increasing strain rate and small voids and cavities were noticed because the stress is higher than a critical stress able to destroy the formed crystals as a result of chain disentanglement.

CHAPTER IV

FABRICATION OF THE PLA/PBT MICROPOROUS FILMS BY BIAXIAL STRETCHING TECHNIQUE

In this chapter, the results and discussion are separated into 2 parts. The first part comprises the investigation of rheological, thermal and dynamic mechanical properties of the PLA/PBT composites before film stretching, and the second part involves the porous structure and thermal behavior of the biaxially stretched films. The film stretching has 2 modes: planar deformation and equibiaxial deformation. Moreover, the methodology to achieve the composites containing differences in size and shape, *i.e.*, sphere and fiber, of PBT in PLA composites is also proposed here.

4.1 Experiment

4.1.1 Materials

PLA (NatureWorks LLC, USA; D-content 4.25% and MFR = 6 g/10 min at 210 °C/2.16 kg) and PBT (Toray and MFR = 26 g/10 min at 250 °C/2.16 kg) were employed in this study. The molecular weight and molecular weight distribution of PLA were analyzed by gel permeable chromatography (GPC) (Tosoh, HPLC-8020). Chloroform was used as eluent at 40 °C at a flow rate of 1.0 ml/min and the concentration of sample was 1.0 mg/ml. The system was calibrated using TSK-GEL® GMHXL as a polystyrene

standard. The number- and weight average molecular weights for as-received PLA are as follows: M_n = 1.07 × 10^5 and M_w = 1.52 × 10^5. Further, the melting temperatures of PLA and PBT determined from a differential scanning calorimeter are 148 and 221 °C, respectively.

4.1.2 Preparation of the PLA/PBT composites

The methodology to achieve the composites containing spherical and fibrous dispersions with difference in particle sizes but identical final composition is illustrated in Figure 4.1. Polymer pellets were dried under vacuum at 80 °C for 4 h to avoid a hydrolytic degradation with moisture. Then, PLA and PBT were mixed in a molten state at various ratios, *i.e.*, 90/10, 75/25 and 60/40 in a volume fraction, using a 60 cm^3 internal batch mixer (Toyoseiki, Labo-plastmil) at 240 °C, which is higher than the melting points of both polymers. Pentaerythritol tetrakis (3-3,5-di-*tert*-butyl-4-hydroxy phenyl propionate) (Ciba, Irganox1010) and tris(2,4-di-tert-butylphenyl)phosphate (Ciba, Irgafos168) as thermal stabilizers were also added at 5000 ppm each to hinder the thermal degradation. The blade rotation speed was 40 rpm and the mixing time was 3 min. The fill factor was 70%. At this step, the dispersion of spherical PBT in PLA matrix was obtained (see results of SEM data).

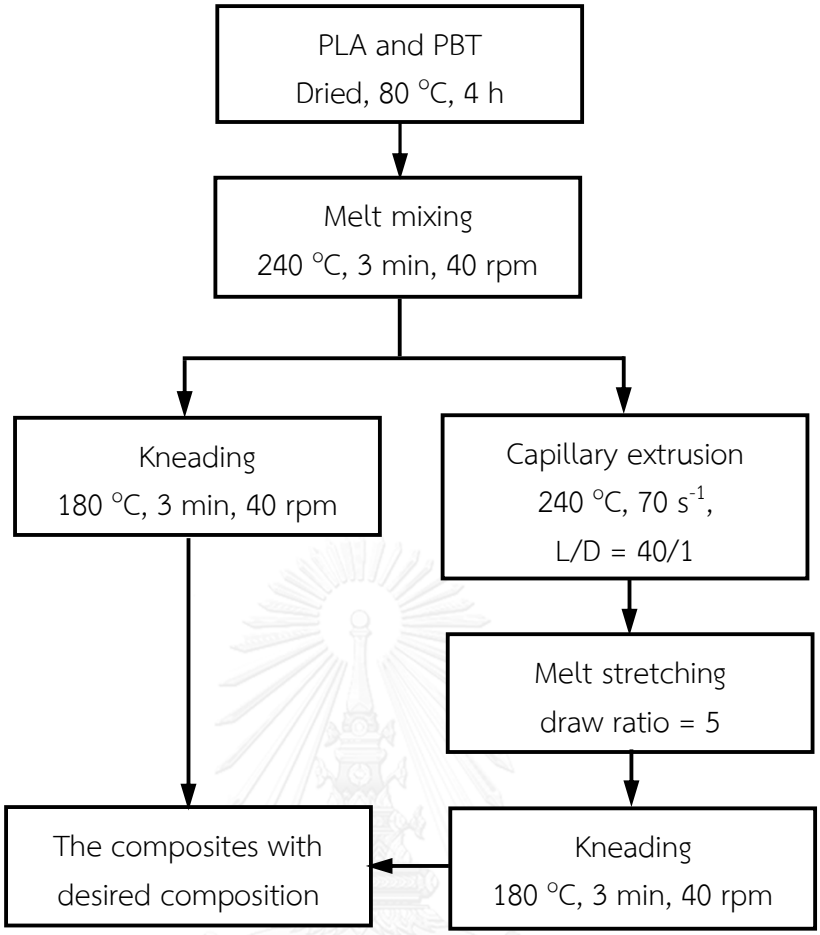

Figure 4.1 Diagram for the preparation method of the PLA composites containing PBT spheres and PBT fibers

In order to prepare the PLA composites containing fibrous PBT dispersion, the aforementioned composites containing spherical dispersion were extruded and then melt-stretched by a pressure-driven capillary rheometer (Yasuda Seiki Seisakusho, 140-SAS-2002) equipped with a circular die having 40 mm in length, 1.0 mm in diameter, and an entrance angle of 180°. The temperature of cylinder and die were at 240 °C, and the applied shear rate was 70 s^{-1}. Subsequently, the extruded strands were melt-stretched by a set of rotating wheels at a draw ratio of 5 and quenched by air flow.

The concentrated composites composed of spherical and fibrous dispersions were diluted by kneading with virgin PLA in an internal batch mixer again at 180 °C, which is above melting point of PLA but lower than the melting point of PBT in order to maintain the shape of PBT, for 3 min to achieve the composites containing spherical PBT dispersion with a final volume fraction of 95/5. Neat PLA was also processed at the same condition for better comparison. The diluted composites were compressed into a flat sheet with a thickness of 200 μm by a laboratory compression-molding machine (Tester Sangyo, SA303IS) at 180 °C under 10 MPa for 3 min, and subsequently cooled down at 40 °C. For simply understanding, the nomenclature used of PLA/PBT composites in this study is summarized in Table 4.1. *SP* and *FIBER* represent the composites containing spherical and fibrous dispersion, respectively, while *S*, *M*, and *L* denote small, medium and large sizes of PBT particles, respectively.

Table 4.1 Nomenclatures of the PLA/PBT composites

Sample code	Type of dispersion	Initial volume ratio
SP-S	Spherical	90/10
SP-M	Spherical	75/25
SP-L	Spherical	60/40
FIBER-S	Fibrous	90/10
FIBER-M	Fibrous	75/25
FIBER-L	Fibrous	60/40

4.1.3 Biaxial film stretching

The stretched films were prepared using a biaxial stretching machine (Imoto Machinery, Biaxial film stretcher IMC11A9) as follows. The compressed sheets were cut into squares of 5 × 5 cm^2 and then clamped by five chucks on each side with the initial distance of 35 mm. The sheets were equilibrated for 40 min at 80 °C, which is about 10 °C higher than the glass transition temperature of PLA. The coordinate system of the film is defined as follows: x- and y- axis is in the in-plane direction and z-axis is in the out-of-plane direction (thickness direction). In *planar deformation*, the sheets were stretched uniaxially in x-direction while the width was kept constant by stretching in y-direction throughout the experiment. In *equibiaxial deformation*, the sheets were simultaneously stretched in x- and y-directions. The stretching modes are showed in Figure 4.2. The stretching speed was 3 mm/s. Moreover, the amount of force in x- and y-directions during film stretching was also recorded. Eventually, the stretched films were held at 80 °C for 10 min to stabilize the porous structure. The stretching ratio (λ) was defined as the ratio of final length to initial length of the films.

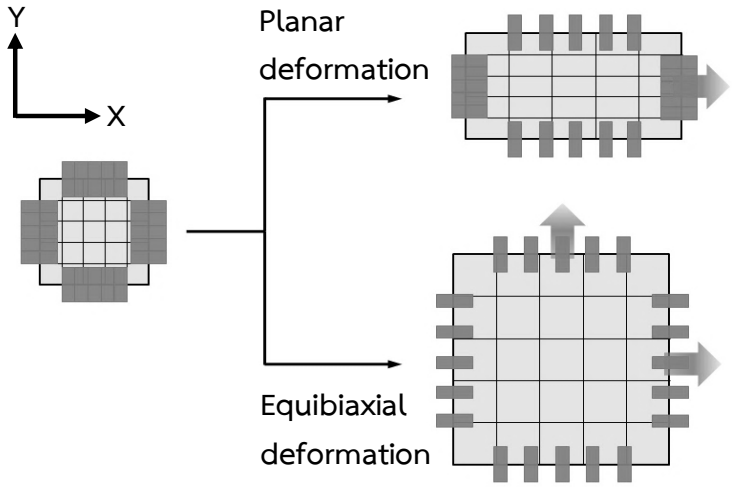

Figure 4.2 Stretching modes employed in this study

4.1.4 Measurements

The steady-state shear viscosities as a function of shear rate for pure PLA and PBT at melt-mixing temperature, *i.e.*, 240 °C, were collected by a capillary rheometer equipped with a circular die (L/D = 40/1). It is suggested that both polymers display the shear-thinning behavior and the shear viscosity of PLA is much higher than that of PBT in an entire range of applied shear rate.

The morphologies of compressed and stretched films were observed by a scanning electron microscope (SEM) (Hitachi, S4100) with an acceleration voltage of 20 kV. The samples were coated with Pt/Pd using an ion sputtering machine (Hitachi, E1010) to increase contrast and reduce charging. PLA phase was removed from the composites by extraction with fresh tetrahydrofuran, which is a good solvent for PLA

but non-solvent for PBT, and the inclusions of insoluble fraction were dropped onto a microscope glass slide and then evaporated. Before SEM measurements, the non-conducting samples were coated with a fine layer of conductive gold using an ion sputtering machine (Hitachi, E1010) to increase electrical conductivity and to prevent charging. To acquire the size and size distribution of PBT inclusions, at least 200 particles per sample were considered to determine the number-average diameter d_n, volume-average diameter d_v and polydispersity *PD* using the following relations:

$$d_n = \frac{\sum n_i d_i}{\sum n_i}$$

$$d_v = \frac{\sum n_i d_i^4}{\sum n_i d_i^3}$$

$$PD = \frac{d_v}{d_n}$$

where n_i is the number of domains with diameter d_i counted from SEM micrographs.

The frequency dependence of oscillatory shear moduli in the molten state, *i.e.*, storage modulus (*G′*) and loss modulus (*G′′*), was measured using a cone-and-plate type rheometer (TA Instruments, AR2000ex) in a frequency sweep mode from 100 to 0.1 rad/s at 180 °C, under a nitrogen atmosphere to minimize thermal-oxidative degradation. The cone angle was 4°, and the diameter was 25 mm.

The temperature dependence of oscillatory tensile responses in the solid state, *i.e.*, storage modulus (*E′*) and loss modulus (*E′′*), were evaluated in an oscillatory tensile mode by a dynamic mechanical analyzer (UBM, E4000) in a temperature range

between -20 and 160 °C with a heating rate of 2 °C/min. The applied frequency 10 Hz, and the oscillation amplitude was 3 μm. The dimension of rectangular specimen cut from the compressed flat sheet was 10 × 5 × 0.2 mm^3.

A differential scanning calorimeter (DSC) (Mettler, DSC820^e) was utilized to collect the thermal properties. Approximately 10 mg in weight of dried samples were encapsulated in standard aluminum pans. The samples were heated from room temperature to 180 °C (1st run) and held for 10 min at 180 °C in order to erase the remaining thermal history. The samples were cooled down to room temperature and heated to 180 °C (2nd run). The heating and cooling rates were 10 °C/min. Further, the degree of crystallinity (X_c) of PLA is calculated by the following relation:

$$X_c = \frac{\Delta H_m - \Delta H_{cc}}{w\Delta H_m^o}$$

where ΔH_m and ΔH_{cc} are the measured enthalpies of melting (from 2nd run) and the cold crystallization, respectively, while ΔH_m^o is the enthalpy of melting for a perfect crystalline PLA (93 J/g) [79]. The w denotes a mass fraction of PLA in the composites.

The stress-strain data in uniaxial tension were obtained by using a tensile testing machine (UBM, S1000-DVE3) equipped with a temperature chamber. The initial distance between the clamps was 10 mm. The rectangular specimens with a width of 10 mm were equilibrated at 80 °C for 5 min and then hot-drawn at a crosshead speed

of 0.05 mm/s (the engineering strain rate was 0.005 s^{-1}). All measurements were performed at least ten times for each formulation.

The density of films was measured according to ASTM D792 [80] using a density kit and a top-loading electronic balance. Distilled water was used as an immersion medium. The dry and wet weights of samples were used to determine the bulk density based on Archimedes's principle as follows:

$$\rho = \frac{W_{air}}{W_{air} - W_{water}} \cdot \rho_{water}$$

where ρ and ρ_{water} are the relative densities of the sample and distilled water, respectively. W_{air} is the weight of sample measured in air and W_{water} is the weight of sample measured in distilled water. The voids were formed after stretching leading to an increase in volume of air inside and a decrease in density. By comparing the difference in density of sample before and after film stretching the void content can be estimated. Triplicates were run for each sample.

Water vapor permeation (WVP) of the PLA/PBT stretched films was determined according to ASTM F1249 [81] using a PERMATRAN-W model 398 (Mocon, USA). WVP value was measured at 37.8 ^{o}C and 90% relative humidity (RH) with a nitrogen flow rate of 250 cm^3/min. The area of the sample was 5 cm^2. The diffused water vapor was detected by a RH sensor.

4.2 Results and discussion

The results and discussion are separated into 2 parts. The first part is the characteristics of the PLA/PBT composites prior to biaxial film stretching, introducing the mechanism of fibrillation of spherical particles into fibrils by capillary extrusion, following by the linear viscoelasticity as well as thermal and dynamic mechanical properties of the composites. The second part involves the microporous films fabricated from the composites obtained from the previous part by biaxial stretching. The effects of morphology of PBT on the porous structure, void content and thermal properties of the biaxially stretched films are discussed.

4.2.1 Characteristics of the PLA/PBT composites prior to film stretching

4.2.1.1 Flow behavior of PLA and PBT during capillary extrusion

It is well studied that the morphology of the binary immiscible blends dominantly depends on the material properties, *i.e.*, viscosity ratio, elasticity ratio, composition, and interfacial tension as well as processing conditions, *i.e.*, nature of flow, mixing temperature and applied shear rate [82]. The steady-state shear viscosities as a function of shear rate for pure PLA and PBT at melt-mixing temperature, *i.e.*, 240 ^{o}C, were collected by a capillary rheometer equipped with a circular die (L/D = 40/1), as shown in Figure 4.3. It is suggested that both polymers display the shear-thinning behavior and the shear viscosity of PLA is much higher than that of PBT in an entire range of applied shear rate.

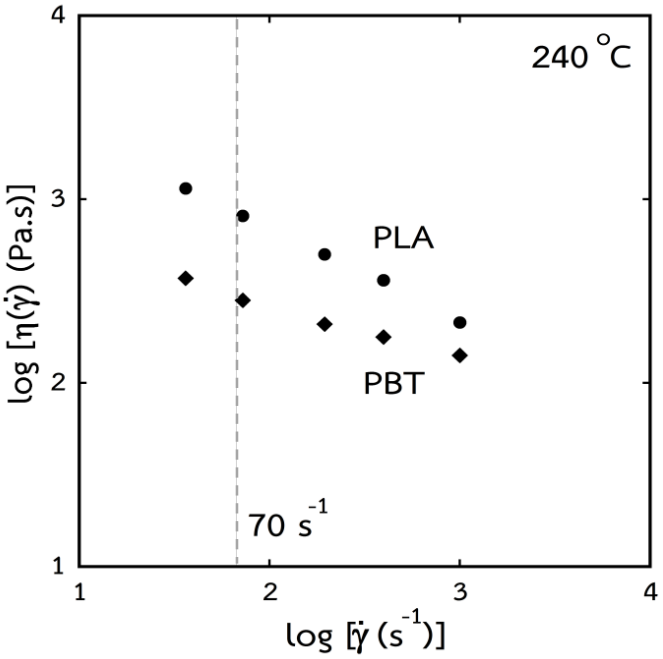

Figure 4.3 Steady-state shear viscosity as a function of shear rate at 240 °C for (circles) PLA and (diamonds) PBT

4.2.1.2 Morphology of dispersed PBT phase in PLA composites

Exemplary SEM micrographs of the extracted PBT inclusions from the PLA composites prior to melt-stretching at various initial compositions are demonstrated in Figure 4.4. The PBT dispersed domains are fairly smooth and perfectly spherical, which is indicative of the immiscibility between PLA matrix and dispersed PBT domains. This type of structure is also known as droplet-matrix morphology. From SEM micrographs

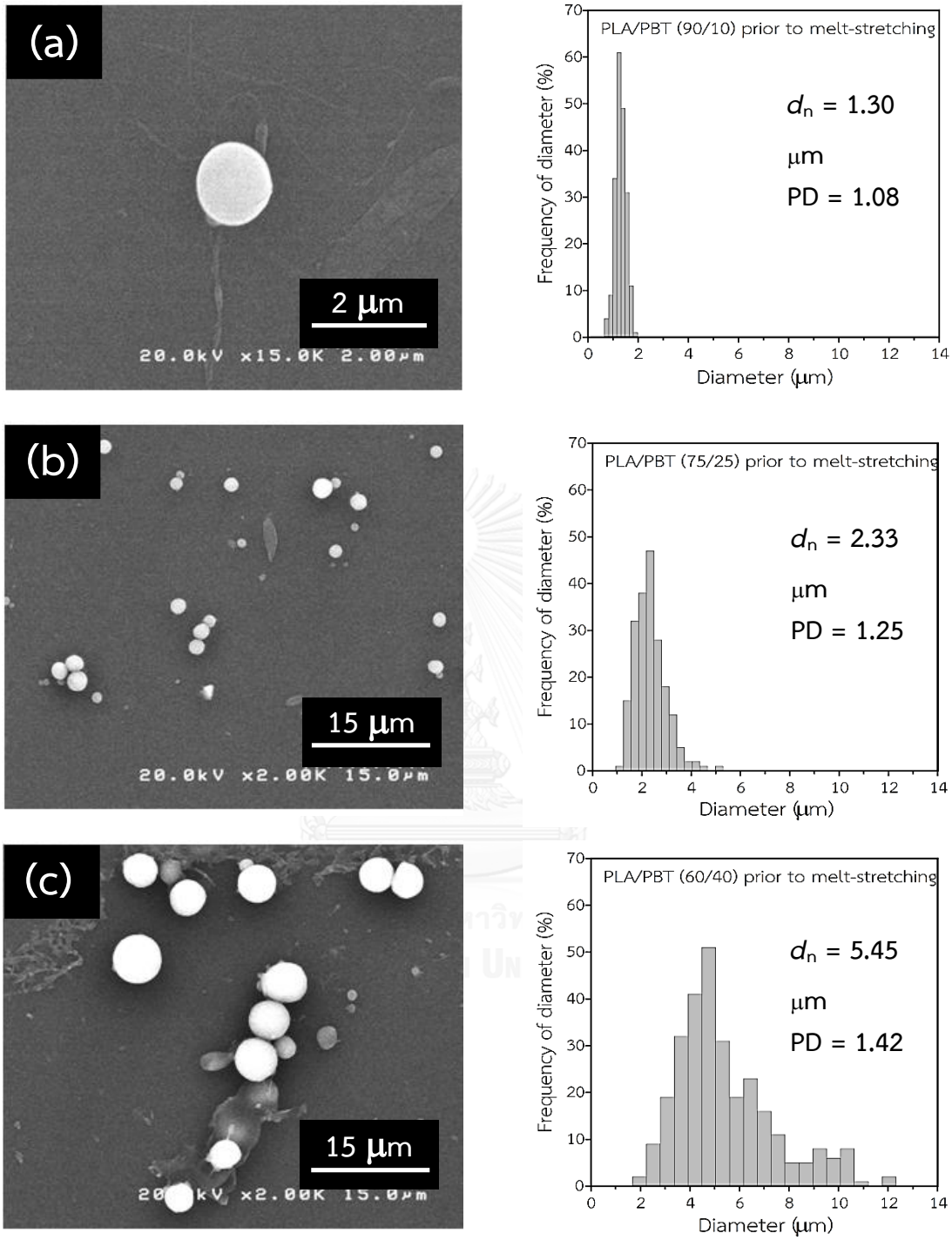

Figure 4.4 SEM micrographs of the extracted PBT domains from the composites prior to melt-stretching for (a) PLA/PBT (90/10), (b) PLA/PBT (75/25), and (c) PLA/PBT (60/40)

the number-average diameter d_n and polydispersity *PD* (in parentheses) of PBT droplets are as follows: 1.30 μm (1.08) for 10 vol% PBT, 2.33 μm (1.25) for 25 vol% PBT, and 5.45 μm (1.42) for 40 vol% PBT. Upon increasing the concentration of the minor phase in the composites, the average particle size of PBT becomes larger and the particle size distribution is broader owing to the favored particle-particle coalescence phenomena of molten PBT droplets caused by flow during melt-mixing process, as illustrated in Figure 4.5 [83].

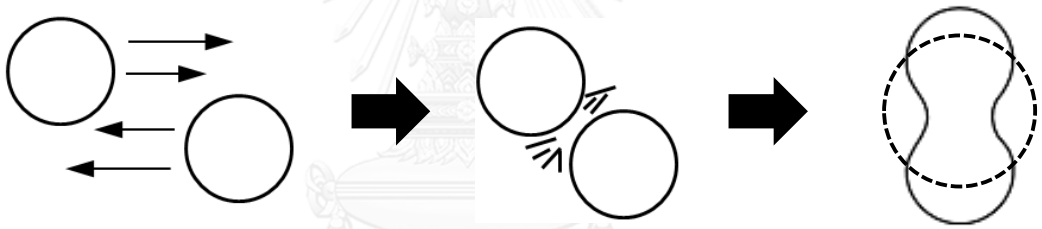

Figure 4.5 Mechanism of coalescence via flow in binary polymer system. Droplets of dispersed phase are collided with each other by shear stress and then formed the equilibrium coalesced droplets (dash line)

During capillary extrusion, the composites were processed under high shear stress in a reservoir at high applied shear rate, thus it is possible that the morphology of the PBT particle will be changed. Generally the evolution of morphology is a result from two competitive mechanisms: breakup and coalescence, and the dimensionless

number that used to explain predict the final morphology of the immiscible blends is capillary number (*Ca*) as defined as follows [84]:

$$Ca = \frac{\dot{\gamma}\eta_m d}{2\Gamma}$$

where $\dot{\gamma}$ is an applied shear rate, η_m is a viscosity of matrix, *d* is the average characteristic diameter of dispersed phase, and Γ is an interfacial tension. *Ca* is a ratio between hydrodynamic forces relating to deformation of dispersed droplets in a shear field and the interfacial forces responsible for keeping the lowest surface energy of the dispersed phase to the equilibrium spherical shape. Considering the composites containing 10 vol% spherical PBT particles with a number-average diameter of 1.30 μm as well as assuming that the interfacial tension between PLA and PBT is about 0.4 mN/m [44], it is found that the capillary number at the applied shear rate of capillary extrusion is 280. In addition, in order for the dispersed phase domains to efficiency breakup into smaller particles, *Ca* must be higher than a critical value (Ca_{crit}), implying that the shear stress on the surface of dispersed particles overcomes the interfacial interaction between the matrix and the dispersed phase. Under elongational flow, a critical capillary number can be calculated using the Grace's empirical equation [85]:

$$\log\left(\frac{Ca_{crit}}{2}\right) = -0.64853 - 0.02442\left(\log\frac{\eta_d}{\eta_m}\right) + 0.02221\left(\log\frac{\eta_d}{\eta_m}\right)^2 - \frac{0.00056}{\log\frac{\eta_d}{\eta_m} - 0.00645}$$

where η_d and η_m stand for steady-state shear viscosities of dispersed phase domain and matrix and found to be 816 and 288 Pa.s, respectively. The calculated Ca_{crit} is 0.46. In our study, $Ca >> Ca_{crit}$ means that the dispersed phase domains change into a filament and then breakup into small droplets.

Furthermore, PBT spheres were transformed into PBT fibers upon capillary extrusion and subsequent melt-stretching, as evidenced by SEM micrographs in Figure 4.6. This kind of structure is called fibrillar morphology. This deformation occurs when the applied shear stress is greater than the interfacial stress, in which tries to keep the dispersed phase in the most equilibrium spherical shape. The deformed particles are drastically elongated by tensile stresses in the stretching direction of the extruded strands and promptly solidified by a cool air. According to the previous literatures [52,86], fast quenching after melt-stretching from the die is important in order to solidify the fibrillar structure, preventing the reverse deformation into sphere. As expected, the diameter of PBT fiber directly corresponds to the original diameter of PBT sphere. The number-average fiber diameter and polydispersity (in parentheses) are as follows: 0.24 μm (1.63) for 10 vol% PBT, 0.62 μm (1.14) for 25 vol% PBT, and 1.99 μm (1.34) for 40 vol% PBT.

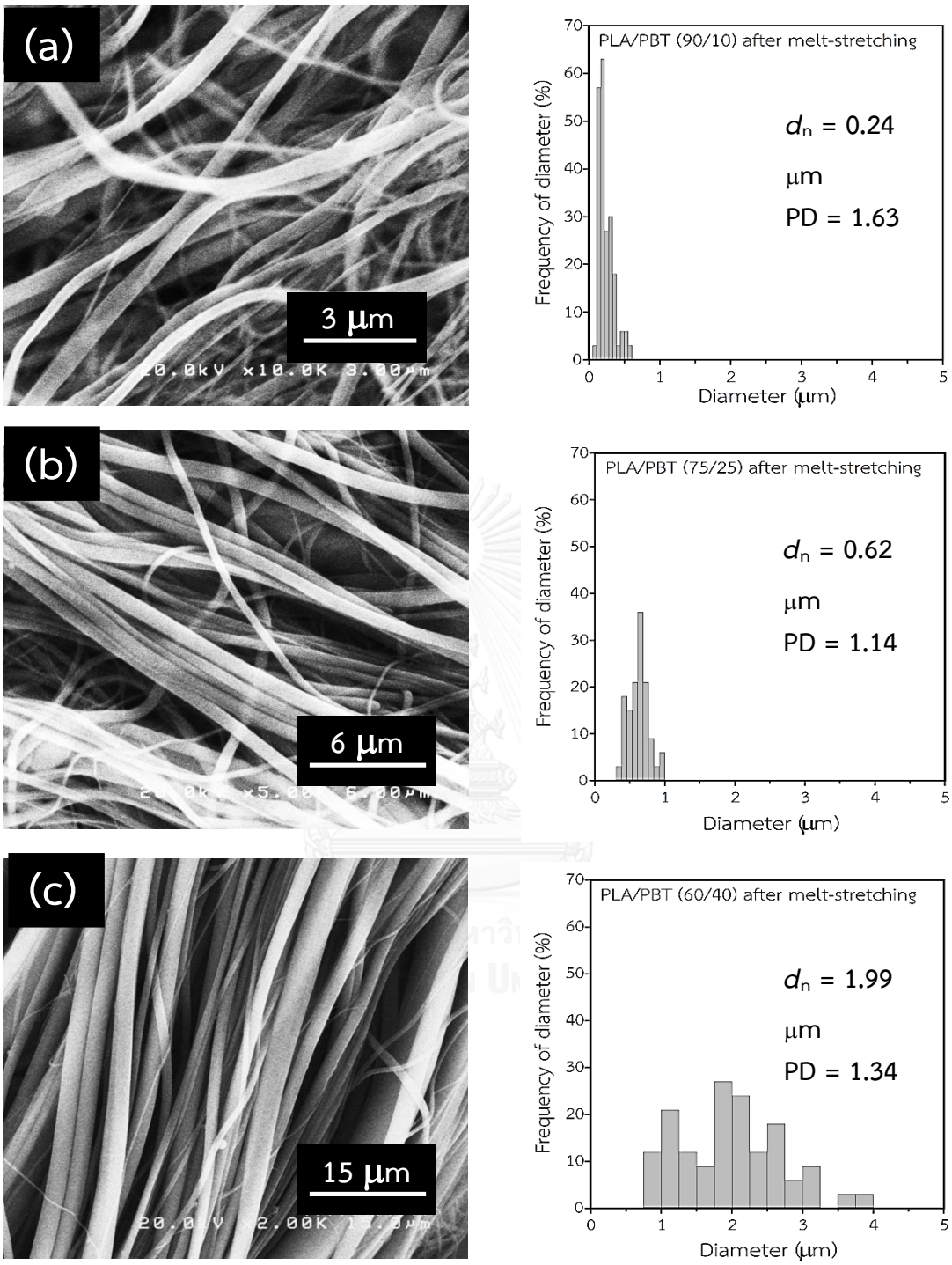

Figure 4.6 SEM micrographs of the extracted PBT domains from the composites after melt-stretching for (a) PLA/PBT (90/10), (b) PLA/PBT (75/25), and (c) PLA/PBT (60/40)

Even though the length of most fibers is still unclear because identifying an individual fiber from the bundles is difficult, Figure 4.7 depicts that it is estimated to be longer than several millimeters and its aspect ratio is expected to be larger than 600. Further, the volume of a fiber seems to be greater than that of a sphere, which is attributed to the coalescence of spherical PBT particles by the contraction flow near the entrance zone of die and shear flow in the die land as illustrated in Figure 4.8 [87,88]. Based on this approximation as shown in equation below, the formation of a fibril results from the coalescence of about 4-5 spherical PBT particles.

$$N\left[\frac{4}{3}\pi\left(\frac{d_{sphere}}{2}\right)^3\right] = \pi\left(\frac{d_{fiber}}{2}\right)^2 L$$

where N is a number of coalesced droplets and L is the length of a fibril.

Finally, it is of particular importance to inform that the concentrated composites before and after melt-stretching are kneaded with plain PLA to dilute into the final volume ratio of 95/5 at the mixing temperature of 180 °C, which is below the melting point of PBT (T_m = 221 °C) but still above that of PLA (T_m = 148 °C), in order to fix the shape and content of PBT in the PLA composites. Moreover, it is worth mentioning that the shape of PBT domains in the PLA composites after kneading with neat PLA at 180 °C is still intact as confirmed by SEM observations.

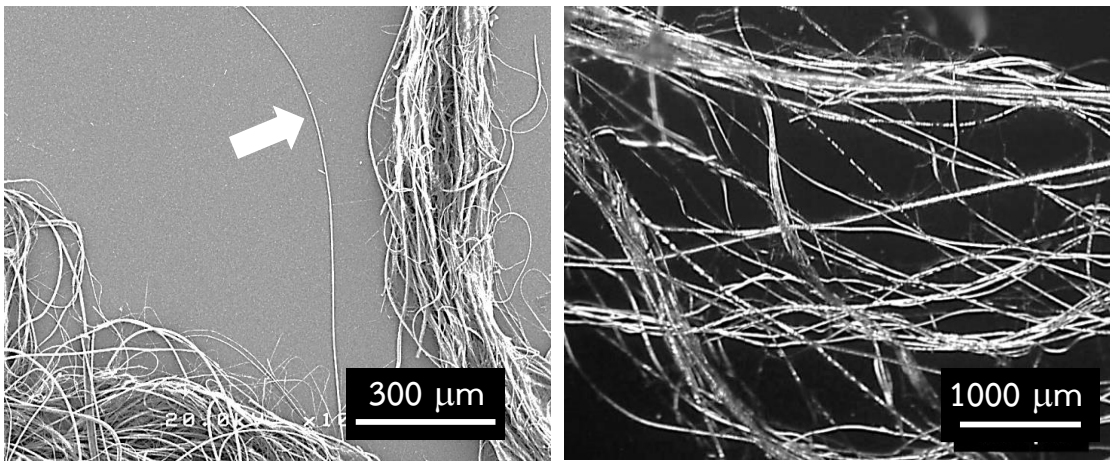

Figure 4.7 SEM and optical images of extracted PBT fibers from the composites

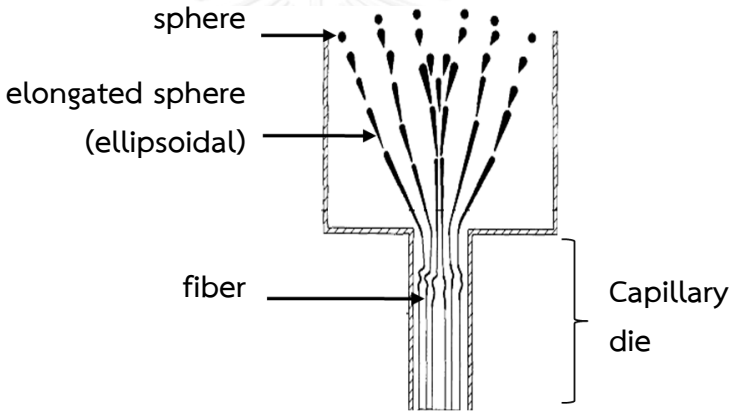

Figure 4.8 Scheme of coalescence and deformation of PBT particles at capillary die

4.2.1.3 Linear viscoelastic behavior of the composites

In order to verify the degradation of materials during measured temperature, the time sweep experiments in a small amplitude oscillatory mode at 240 °C and 10 Hz as shown in Figure 4.9. Shear storage modulus (G') and complex viscosity (η^*) of PBT are almost constant, indicating that PBT was thermally stable; however, in spite of being operated under nitrogen atmosphere and dried before experiment to remove

a scarce of moisture residue, slight decreases in G' and η^* for PLA are observed after 4 min at the measured temperature. Thus, the analysis of rheological properties for PLA and their composites were measured at an angular frequency range of 100-0.1 rad/s (measurement time = 7 min) and several specimens were used to reduce the time of thermal exposure and to avoid the effect of thermal degradation.

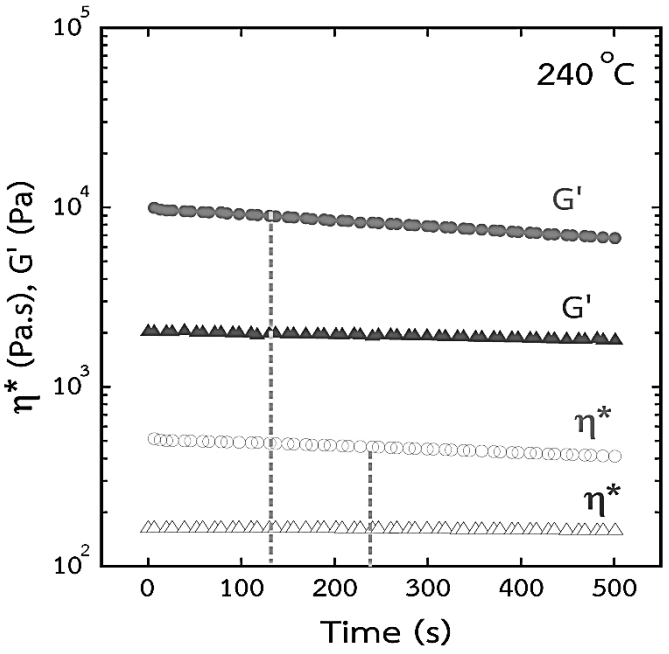

Figure 4.9 Time sweep experiments of PLA (circles) and PBT (triangles) at 240 °C and 10 Hz. The dash lines show the reduction of G' and η^* of PLA by 10%

The linear viscoelastic responses give the reliable information on the microstructure development in polymer systems. Figure 4.10 depicts the frequency dependence of oscillatory shear modulus G' and loss modulus G'' at 200 °C plotted against angular frequency for neat PLA and the composites with dispersed PBT, in

which PBT exists in the solid state. The slopes of G' and G'' curves for PLA close to 2 and 1 at low frequencies, respectively, indicating that viscous flow is predominant in the terminal zone with the characteristic of a linear viscoelastic fluid [89]. The zero-shear viscosity for PLA is calculated to be ~6.6×10^2 Pa s at 200 °C.

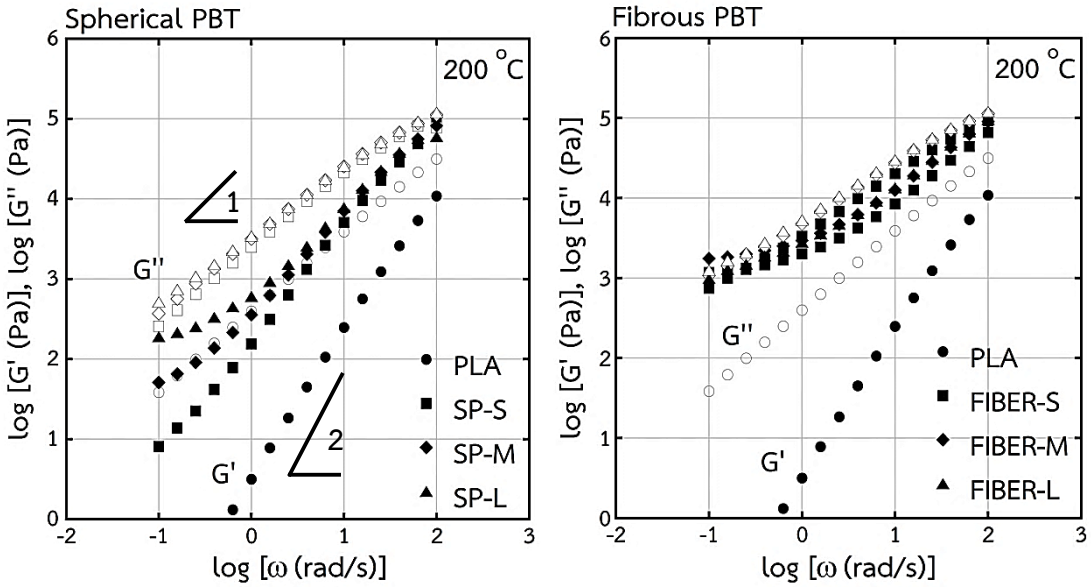

Figure 4.10 Frequency dependence of (closed symbols) shear storage modulus G' and (open symbol) loss modulus G'' at 200 °C for neat PLA and its composites

There are two reasons to describe an improvement of G' for the composites. One is the rigidity effect of filled particles and the modulus of the composites which contain rigid spherical particles can be estimated by many elaborate equations such as Kerner's equation as given below [90]:

$$\frac{G_c}{G_m} = 1 + \frac{15(1-\nu_m)}{8-10\upsilon_m}\frac{\phi_d}{(1-\phi_d)}$$

where G_c and G_m are the moduli of composites and matrix, υ_m is the matrix Possion ratio, and ϕ_d is volume fraction of dispersed phase. The equation predicts a 12% increase in G' of composites containing 5 vol% spherical PBT particles. Although Kerner's equation neglects the effect of particle size, recent studies [67,69] have reported that the modulus of micro-particulate composites is unaffected by particle size at low particle loading, except for those containing nanoparticles [66,68].

Therefore, the improvement of the G' for the PLA/PBT composites can be explained by the lubrication effect of the particles prolonging the relaxation time of the particle via the shape recovery phenomenon during an oscillatory shear deformation [89]. Furthermore, a secondary plateau in the G' curve in the low-frequency region is clearly observed as the PBT particle size becomes larger since they require longer relaxation time to relax the interaction between interspacing particles. This phenomenon is pronounced as the content of PBT increases (results not presented here). Specifically, the secondary plateau region is clearly observed at lower frequencies for the composites composed of fibrous PBT, which is attributed to the existence of network structure of random interdigitation of dispersed PBT fibers formed upon kneading process.

4.2.1.4 Tensile properties at 80 °C of the composites

The engineering stress-strain curves for pure components and the composites stretched in a uniaxial direction in the rubbery state of PLA at 80 °C are demonstrated in Figure 4.11 and 4.12. This temperature is for biaxial film stretching in the next section (details will be informed later). The initial slope of the curve in the elastic region is the Young's modulus of materials, which represents the mechanical strength of materials to deform. It is found that PLA and PBT have Young's moduli of approximately 2.2 and 250 MPa, respectively, implying that dispersed PBT domains behave like a rigid particles in the PLA composites at this temperature. Hence, the tensile stress and Young's modulus are raised when the PBT particles are presence in the composites.

Moreover, the size of the PBT particles shows insignificant difference in an enhancement of Young's modulus. It should be interestingly noted, however, that the tensile stress for the composites containing fibrous dispersion gradually increases without plateau like for those containing spherical dispersion, indicating the marked strain hardening behavior because of the network structure of a random orientation of PBT fibers in the samples hindering the mobility of PLA chains as well as fibrous PBT themselves. Furthermore, the magnitude of strain hardening behavior for all composites containing fibrous dispersion seems to be unrelated to the size of fiber, which hints that the degree of network entanglement of fibers is almost identical.

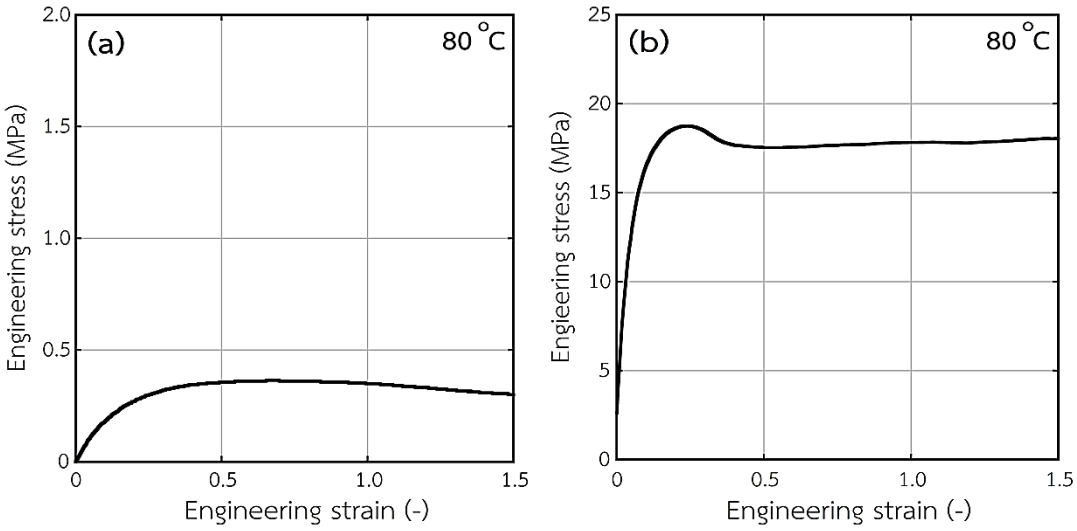

Figure 4.11 Engineering stress-strain curves in tensile mode at 80 °C for (a) neat PLA and (b) neat PBT

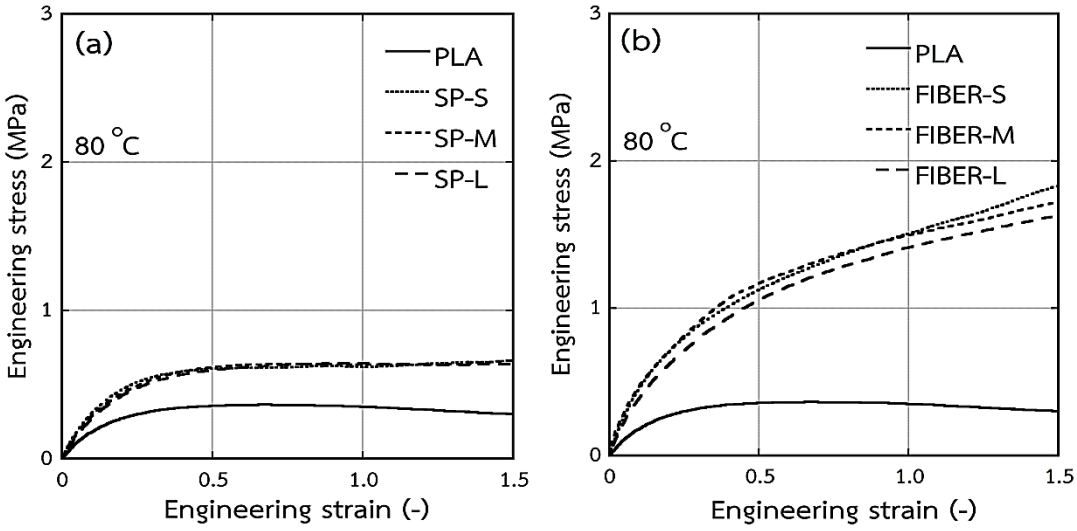

Figure 4.12 Engineering stress-strain curves in tensile mode at 80 °C for the PLA/PBT composites containing (a) spherical dispersion and (b) fibrous dispersion

4.2.1.5 Dynamic mechanical properties of the composites

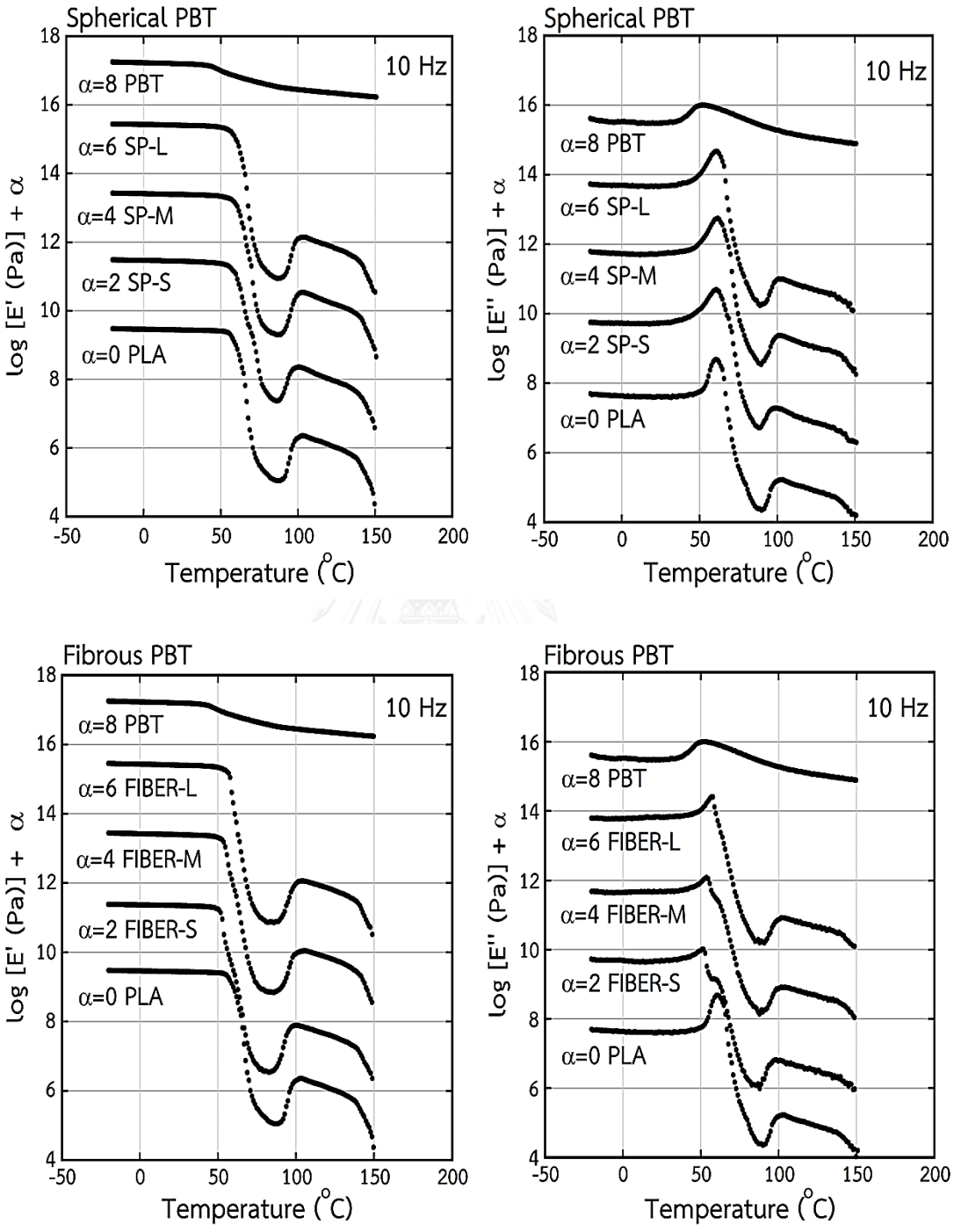

Figure 4.13 Temperature dependence of tensile storage modulus *E′* and loss modulus *E′′*at 10 Hz for neat PLA, neat PBT and its composites

Figure 4.13 exemplifies the temperature dependence of oscillatory tensile moduli such as storage modulus *E′* and loss modulus *E″* in the solid state at 10 Hz for neat PLA, neat PBT and the composites with 5 vol% of PBT. The storage modulus *E′* at room temperature of PLA (3.01 GPa) is higher than that of PBT (1.79 GPa), indicating that PLA has higher rigidity than PBT at glassy state. As the temperature increases, the *E′* falls off sharply around at 60 °C associated with the glass-rubber transition of PLA phase. The *E′* increases to an even great extent in a temperature range of 85-100 °C because the PLA chains reorganize from the glassy state into a crystalline structure at a nanometer level. This crystalline formation from the glassy state is called *cold crystallization* [91], which has always found in slow crystallizing polymers like PLA and PET as they are suddenly quenched due to the cooling condition of compression-molding machine, *i.e.*, 40 °C. After that, the material follows the rubbery plateau region in which the polymer chains can microscopically rotate or move in the deformation direction and finally reach the flow region where the crystals are completely melted.

It should be noted that the *E′* in rubbery region, *i.e.*, at 80 °C (which is a film stretching temperature in this study), for PBT (387 MPa) is much higher than that for PLA (0.18 MPa), suggesting that the dispersed PBT domain behaves like rigid particle under film stretching condition. It is also mentioned that the peak of cold-crystallization, indicated by the inserted bold arrows, is insensitive to the size of spherical PBT; however, the cold crystallization shifts to lower temperature in case of incorporating fibrous PBT, suggesting that fibrous PBT can significantly accelerate the

cold crystallization rate of PLA matrix. Moreover, the peak in the *E''* curve, ascribed to the glass transition temperature (T_g), demonstrates the doublet peaks for the composites containing fibrous PBT, whereas these separated peaks are hardly seen for the composites containing spherical PBT. The two individual peaks at lower and higher temperatures are the contribution of PBT (52 °C) and PLA (70 °C), respectively. It is deduced from the results that the PLA/PBT composites show phase separation and the immiscibility is obviously seen for the composites containing fibrous PBT owing to the difficulty for fibrils to dissolve into the PLA matrix, which is presumably attributed to the agglomeration of entanglement of PBT fibers.

4.2.1.6 Thermal properties of the composites

In order to elucidate effects of size and shape of PBT on the cold crystallization, the thermal properties are evaluated by DSC in a dynamic sweep mode under nitrogen purge as illustrated in Figure 4.14. After removing the thermal history and cooling down to room temperature, the specimens were heated again to measure the thermal properties. The no shift of glass transition temperature at 60 °C for PLA confirms the phase-separated morphology, corresponding to the DMA and SEM results. Comparing with PLA curve, the exothermic cold crystallization peaks are slightly shifted downward when the PBT spheres are added and considerably in case of an addition of PBT fibers. It is possible that PBT acts as a nuclei site for PLA chains to reorganization into a crystal

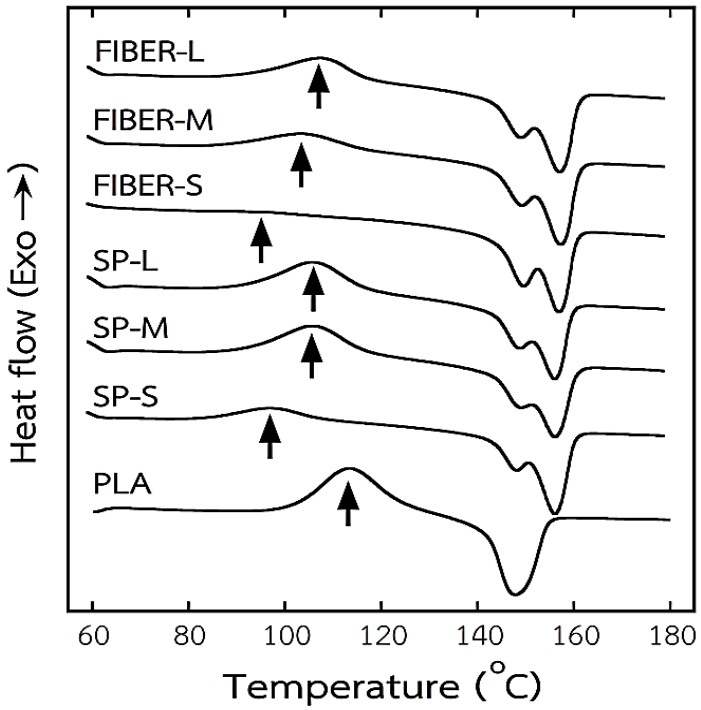

Figure 4.14 Dynamic DSC second heating thermograms of neat PLA and its composites at a scan rate of 10 °C/min. The inserted bold arrows indicate the cold crystallization

structure as the required energy is high enough during heating scan. Particularly, the enhancement of cold crystallization is more pronounce when the diameter of the dispersed PBT particles became smaller, which can be explained by the higher interfacial area between surface of PBT particles and PLA matrix. In addition, a single sharp endothermic peak around 148 °C is attributed to the characteristic melting temperature of PLA. Nevertheless, the existence of double endothermic melting peaks is found, which could be a contribution of the presence of disordered crystal system

(α′-form) and then the rearrangement to the more perfect crystalline (α-form) at higher temperature during the DSC heating scan.

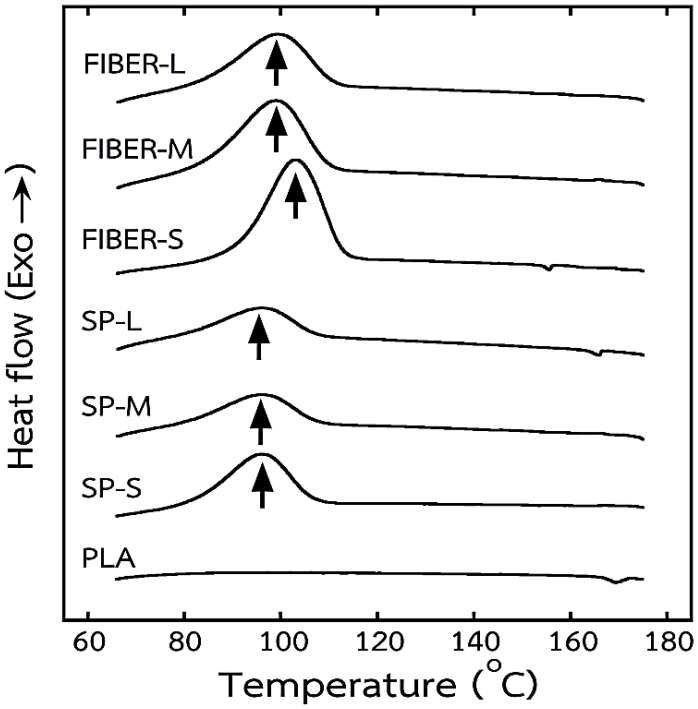

Figure 4.15 Dynamic DSC cooling thermograms of neat PLA and its composites at a scan rate of 10 °C/min. The inserted bold arrows indicate the crystallization

For the DSC cooling scan as depicted in Figure 4.15, the exothermic crystallization peak of PLA is absent, pointing out that the cooling rate is too fast, thus PLA chains in the molten state are rapidly quenched and do not have enough time to self-adjust into a crystalline form, leading to an amorphous phase. On the other hand, appearance of the crystallization is detected when PBT particles are incorporated in

the composite systems because PBT has the nucleating ability to promote the crystallization of PLA. This improvement of cold-crystallization and crystallization of PLA were also reported in case of incorporating other polyesters, *i.e.*, poly(ethylene terephthalate) (PET) [92] and poly(butylene succinate) (PBS) [39]. The thermal properties are summarized in Table 4.2.

Table 4.2 Thermal properties of neat PLA and PLA/PBT composites obtained from cooling and second heating scans[a]

	Cooling scan		Second heating scan					
Sample	T_c (°C)	ΔH_c (J/g PLA)	T_{cc} (°C)	ΔH_{cc} (J/g PLA)	T_{m1} (°C)	T_{m2} (°C)	ΔH_m (J/g PLA)	X_c (%)
PLA	—	—	117.5	23.4	147.9	—	26.6	3.5
SP-S	96.1	11.9	96.7	7.6	148.1	156.1	25.2	18.9
SP-M	96.2	5.1	105.6	13.0	149.2	156.2	25.9	13.9
SP-L	95.8	4.6	106.0	17.0	148.9	156.0	23.6	7.2
FIBER-S	103.3	21.4	95.2	0.8	149.7	156.8	29.1	30.4
FIBER-M	99.0	11.9	103.8	9.3	149.4	157.3	27.3	19.4
FIBER-L	99.4	9.1	107.1	11.1	149.0	157.0	26.9	17.1

[a] The subscripts *c, cc, m* represent crystallization, cold crystallization, and melting, respectively.

4.2.2 Porous structure and thermal properties of the stretched films

4.2.2.1 Surface morphology and void content of stretched films

The film stretching is performed at the temperature beyond the glass transition temperature of PLA (~70 °C), which is in the rubbery region of PLA. It is important to point out that the film stretching cannot be carried out below 80 °C since the sheet specimens start to tear off around the chucks at a low strain level. Figure 4.16 and Figure 4.17 exemplifies the engineering stress-strain curves at 80 °C during biaxial film stretching. Assuming the composites have no voids prior to stretching, the void content can be quantitatively approximated by comparing the apparent bulk density of the specimens before and after film stretching.

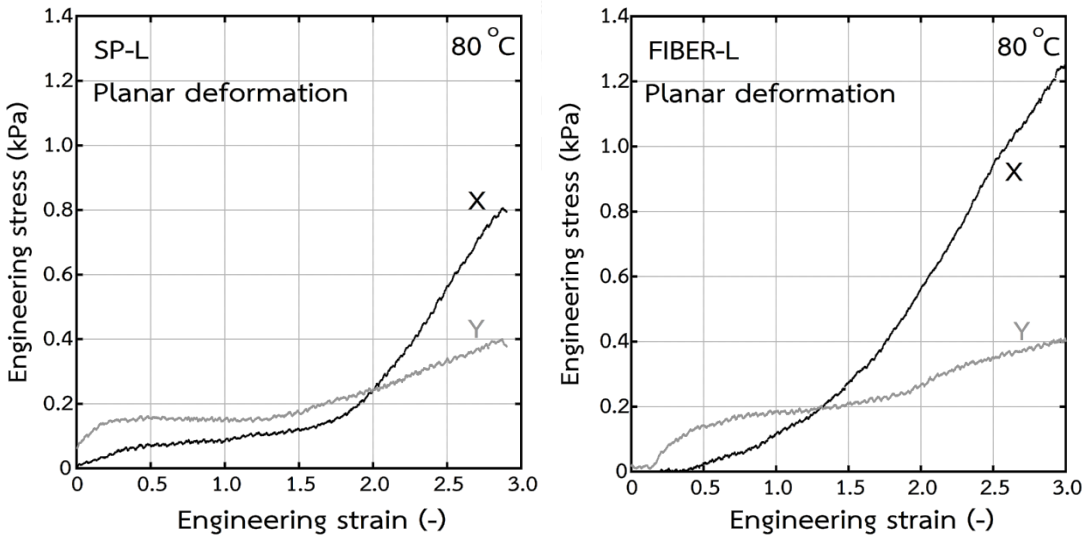

Figure 4.16 Engineering stress-strain curves at 80 °C of SP-L and FIBER-L prepared by planar deformation

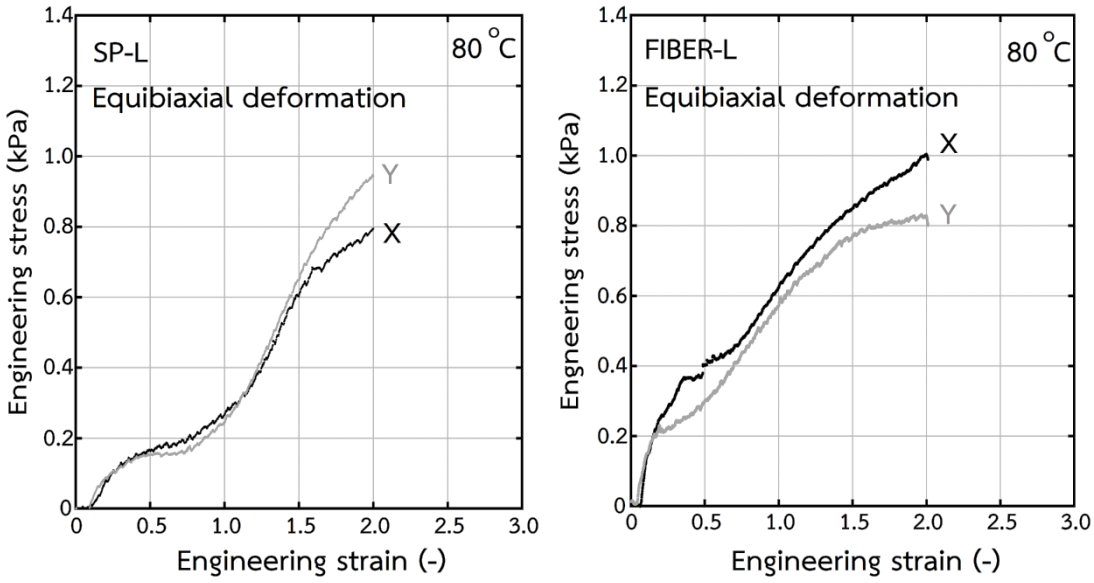

Figure 4.17 Engineering stress-strain curves at 80 °C of SP-L and FIBER-L prepared by equibiaxial deformation

SEM images of the stretched films are shown in Figure 4.18. It is described that during deformation of heterogeneous system, the dispersed phase acts as stress concentrator leading to a local increase in an intensity of actual stress distribution in their vicinity, which is higher than the nominal stress, irrespective of the value of applied load. Although the voids are not observed at $\lambda_x \times \lambda_y = 2 \times 1$, the ellipsoidal voids markedly expands at the polar region of the particles in the stretching direction at $\lambda_x \times \lambda_y = 4 \times 1$. This is because the actual stress concentration in the vicinity of dispersed PBT is intensified because it acts as stress concentrator, and the void opening occurs when the local stress overcomes the interfacial adhesion between PBT domains and PLA matrix. Theoretical speaking, the weak interfacial adhesion in the immiscible blends is favorable for the debonding at the particle-matrix interface.

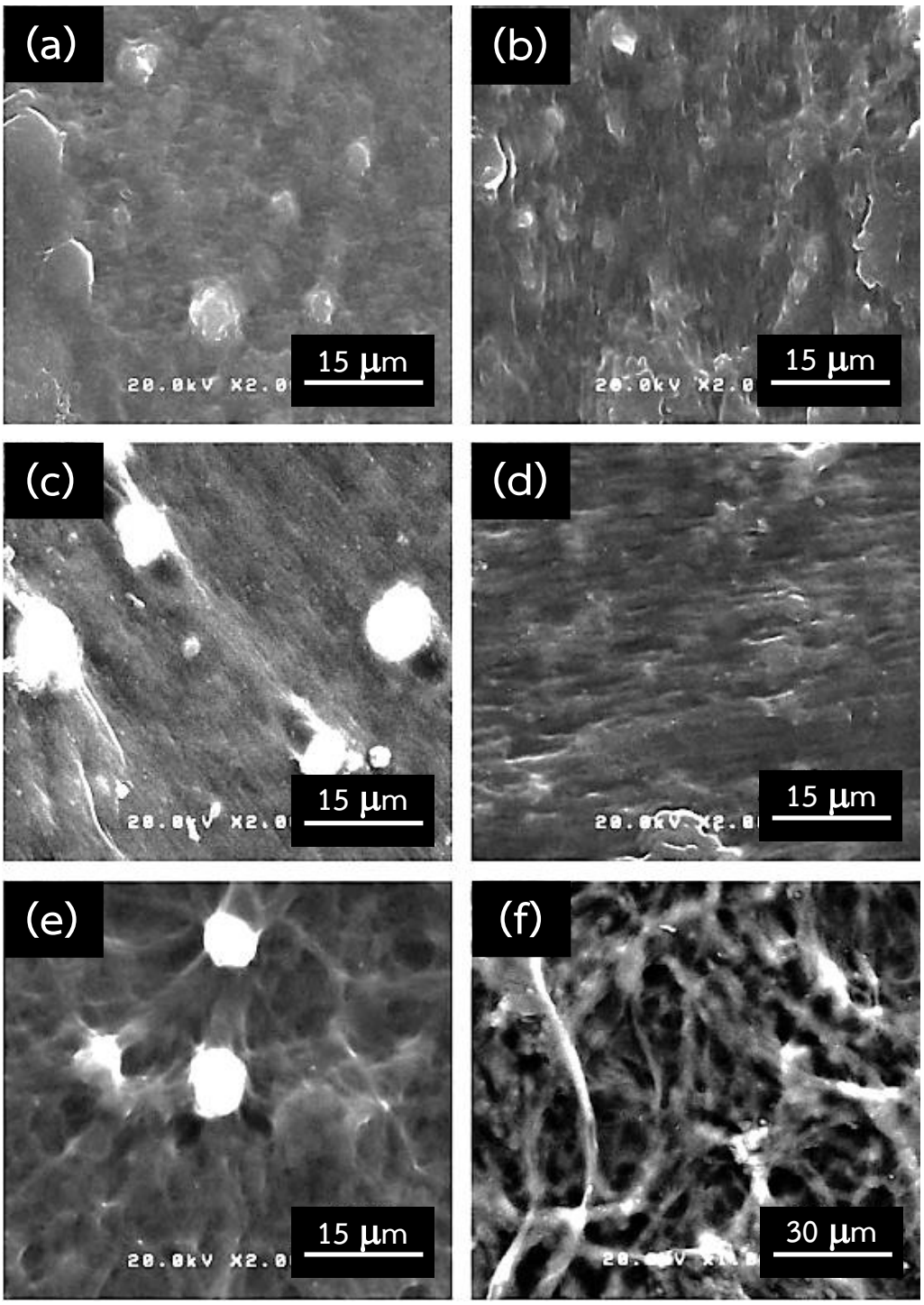

Figure 4.18 SEM images of the surface of the PLA/PBT stretched films: (a) SP-L, $\lambda_x \times \lambda_y = 2 \times 1$; (b) FIBER-L, $\lambda_x \times \lambda_y = 2 \times 1$; (c) SP-L, $\lambda_x \times \lambda_y = 4 \times 1$; (d) FIBER-L, $\lambda_x \times \lambda_y = 4 \times 1$; (e) SP-L, $\lambda_x \times \lambda_y = 3 \times 3$; (f) FIBER-L, $\lambda_x \times \lambda_y = 3 \times 3$

Table 4.3 Void content of the PLA/PBT stretched films containing various diameters of PBT dispersed domain. The stretching ratio is $\lambda_x \times \lambda_y = 4 \times 1$

Sample	PBT diameter (μm)	Void content (%)	Pore shape	Average pore size (μm)
SP-S	1.30	1.73 ± 0.23	ellipsoid	0.91
SP-M	2.33	2.11 ± 0.48	ellipsoid	1.46
SP-L	5.45	1.72 ± 0.99	ellipsoid	3.34
FIBER-S	0.24	0.46 ± 0.18	n/a[a]	n/a
FIBER-M	0.62	2.80 ± 0.19	slit	0.32 (width) × 2.57 (length)
FIBER-L	1.99	4.96 ± 0.54	slit	0.82 (width) × 4.63 (length)

[a] not available

In planar deformation, it should be noted that there is a correspondence between the pore size and size of dispersed PBT sphere size, as shown in Table 4.3. For instance, the average pore size is approximately 0.91 and 3.34 μm for the SP-S and SP-L stretched films, respectively. According to the energy balance between the stored elastic energy and the surface free energy of the spherical particles, the minimum required stress to initiate the cavity around the dispersed particles, is *debonding stress* σ_{db} shown as follows [93]:

$$\sigma_{db} \propto \left(\frac{EW_a}{D}\right)^{1/2}$$

where E is Young's modulus, W_a is work of interfacial adhesion, and *D* is diameter of dispersed particle. This relationship suggests that the debonding effect is more pronounced for larger particle size since the stress concentration directly relates to the particle size. However, the void contents in Figure 4.19 are in the same order of magnitude (~2 %), implying that the number of void in the SP-S stretched films is probably higher than those in SP-M and SP-L stretched films. On the contrary, the stretched films containing fibrous PBT exhibited a lot of needle-like microvoids on the film surface with a void content of ~5 % at $\lambda_x \times \lambda_y = 4 \times 1$. An average pore size is approximately 0.82 μm in width and 3-5 μm in length. Further, the stretched films prepared by equibiaxial deformation ($\lambda_x \times \lambda_y = 2 \times 2$) contain less void content than those prepared by planar deformation ($\lambda_x \times \lambda_y = 4 \times 1$) at the same stretching level. Moreover, the void content for composites containing fibrous dispersion markedly increases to about 8 % at $\lambda_x \times \lambda_y = 3 \times 3$, as demonstrated in Figure 4.20.

In a fibrous system, fibers entangle with neighboring fibers upon mixing resulting in the formation of random network structure, as evidenced by an increase in oscillatory storage moduli in the low-frequency region shown in Figure 4.10. In the mechanics point of view, the flexible fibers generally store the strain energy in a form of extensional deformation. As can be seen in the stress-strain curves in Figure 16 and

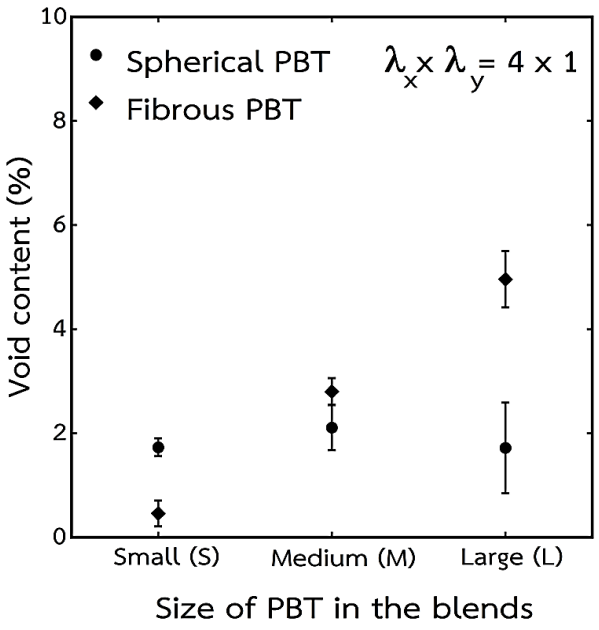

Figure 4.19 Void content as a function of particle size from the PLA/PBT films stretched at $\lambda_x \times \lambda_y = 4 \times 1$

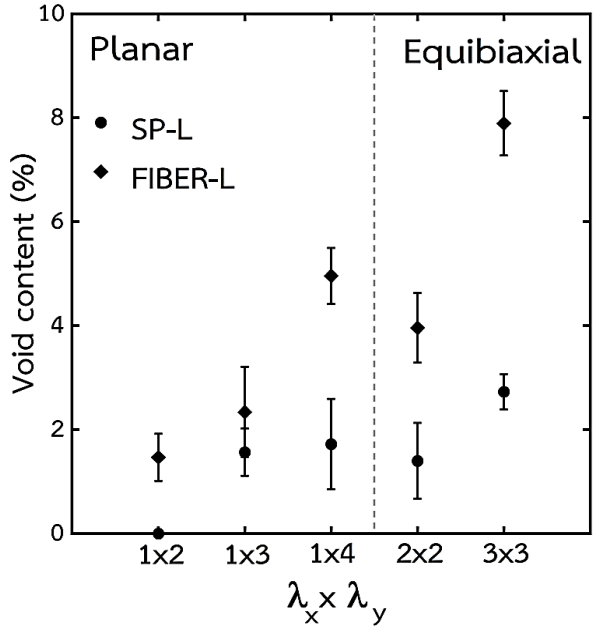

Figure 4.20 Void content as a function of $\lambda_x \times \lambda_y$ from the PLA/PBT stretched films: (circles) SP-L, and (diamonds) FIBER-L

Figure 4.17, an increase in a level of stress during film stretching is obviously begun at high stretching ratio, indicating that the deformation is restricted and much level of energy is required because the discrete entanglements of fibers, which behave like physically crosslinked points, constrains the mobility of polymer chains to freely move from a specified position. Therefore, this inherently non-affine behavior is prominent for the composites containing flexible PBT fine fibers in comparison with those with spherical PBT droplets [94]. Additionally, a large number of crosslinked points provide areas with higher stress concentration than the surrounding polymer matrix and it is expected that a localized deformation between these fibers is the origin of the void formation in this study.

4.2.2.2 Thermal behavior under stretching

The thermal properties of the stretched films are also important and Figure 4.21 illustrates the DSC heating curves of the stretched films produced at distinct stretching ratios. During both planar deformation and equibiaxial deformation, the shifts of cold crystallization temperature to lower temperatures and the disappearance of heat of cold crystallization at high stretching ratios suggesting that PLA chains in amorphous phase begin to align in the stretching direction and, eventually, thermally or mechanically crystallize as a result of a strain-induced crystallization, leading to the higher crystallinity.

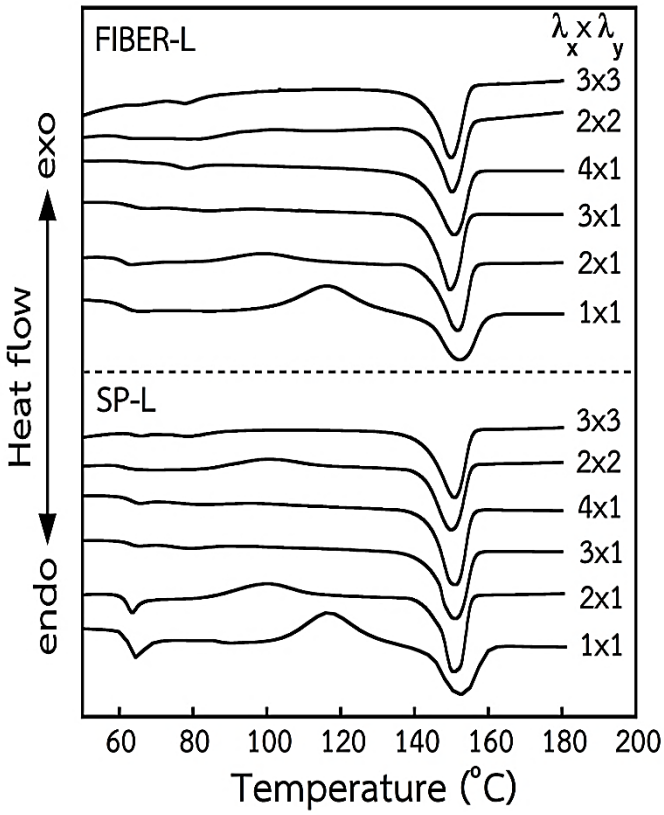

Figure 4.21 DSC curves of the PLA/PBT stretched films

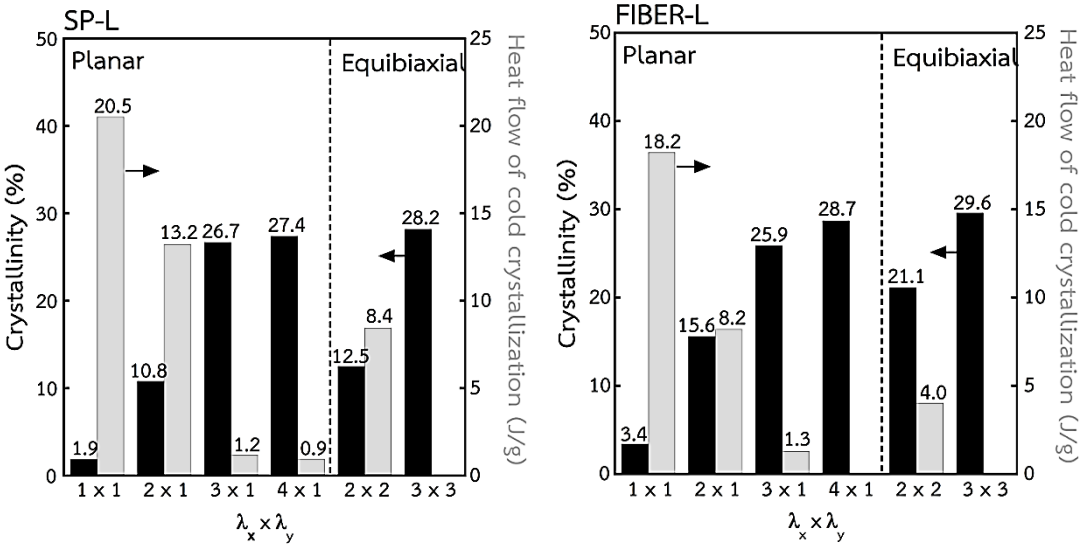

Figure 4.22 Crystallinity and heat flow of cold crystallization as a function of $\lambda_x \times \lambda_y$ for the PLA/PBT stretched films: (a) SP-L, and (b) FIBER-L

As seen in Figure 4.22, crystallinity substantially increases for the planar deformation at low deformation levels, *i.e.*, $\lambda_x \times \lambda_y = 2 \times 1$, because of the mobility of molecular chain segments; however, increasing the stretching ratio gives a gradual increase in crystallinity since the neighboring crystalline structures acting as a type of physical crosslink restrict the relaxation of polymer chains and segments in the non-crystalline region [95]. Further, the composites with fibrous PBT exhibit slightly lower heat of cold-crystallization and increased crystallinity because fibrous PBT can promote the crystallization process more effectively than spherical PBT. The mechanisms of strain-induced crystallization in planar and equibiaxial deformation are illustrated in Figure 4.24 and Figure 4.25.

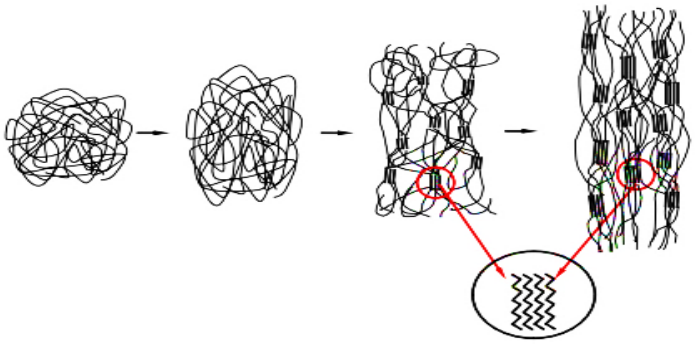

Figure 4.23 Development of crystalline structure for planar deformation [74]

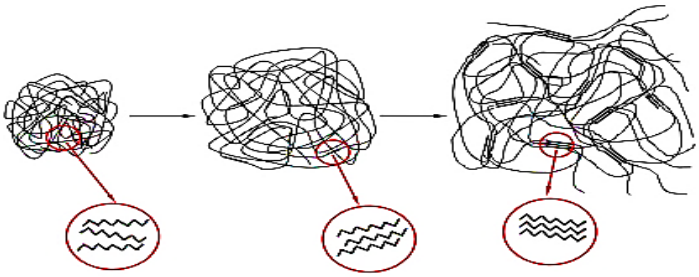

Figure 4.24 Development of crystalline structure for equibiaxial deformation [74]

4.2.2.3 Water vapor permeation of the PLA/PBT stretched films

The water vapor permeation (WVP) test of the PLA/PBT stretched films is also performed to evaluate the performance of the microporous films. WVP values of the unstretched films and biaxially stretched films are summarized in Table 4.4.

Table 4.4 Water vapor permeation for the PLA/PBT unstretched and stretched films

Sample	Film thickness (mm)	$\lambda_x \times \lambda_y$	Water vapor permeation (gm.mil/m^2.day)
Neat PLA	0.200	1 × 1	231.01
SP-L	0.200	1 × 1	363.36
FIBER-L	0.200	1 × 1	376.45
SP-L	0.110	4 × 1	748.96
FIBER-L	0.110	4 × 1	878.32
SP-L	0.080	3 × 3	760.22
FIBER-L	0.080	3 × 3	1038.53

As displayed in Table 4.4, WVP value of compressed neat PLA is about 231.01 gm.mil/m^2.day. The WVP results are significantly consistent with the void content demonstrated in Figure 4.20. Namely, WVP value increases as the stretching level becomes larger because the water vapor molecules pass through a lot of small voids formed upon mechanical stretching of the PLA/PBT microporous films. The FIBER-L

films biaxially stretched at $\lambda_x \times \lambda_y = 3 \times 3$ show the highest WVP value of 1038.53 gm.mil/m^2.day. Accordingly, this data confirms that the biaxial film stretching is a potential technique to fabricate the PLA/PBT microporous films.

CHAPTER V

ISOTHERMAL CRYSTALLIZATION KINETICS AND MORPHOLOGY OF THE PLA/PBT COMPOSITES

Herein, the effects of shape and size of dispersed PBT domains on the crystallization kinetics and development of crystalline structure of PLA under isothermal condition are comparatively examined.

5.1 Experiment

5.1.1 Materials and samples preparation

The commercially available poly(lactic acid) (PLA) and poly(butylene terephthalate) (PBT) were chosen as matrix and dispersed phase, respectively. The specification of PLA and PBT are as same as reported in Chapter IV. The composites were prepared following the procedure in the previous section; (1) melt-mixing at 240 ^{o}C to obtain the composites containing spherical dispersion, (2) capillary extrusion at 240 ^{o}C to produce fibrillar morphology, and (3) kneading with neat PLA at 180 ^{o}C to dilute the composition without fluctuating the shape of dispersed PBT domains. The final volume ratio of PLA to PBT in the composites is 95/5.

5.1.2 Isothermal crystallization kinetics by DSC

The isothermal crystallization behavior and kinetics of neat PLA and its composites were investigated by differential scanning calorimetry (DSC) (Perkin-Elmer, Pyris Diamond DSC) under a nitrogen purge at a flow rate of 50 ml/min through the DSC cell to minimize thermal degradation. Baseline was recorded before measurements and empty pan was used as reference. Approximately 10 ± 0.2 mg in weight of dried samples were encapsulated in 50 μl standard aluminum pans, and each sample was analyzed only once to prevent the effect of thermal degradation. Samples were heated from room temperature to 180 °C at a rate of 80 °C/min and kept at this temperature for 10 min afterwards to eliminate any thermal history and in that way the remaining crystalline of PLA as nucleation site. Samples were rapidly cooled at a rate of 40 °C/min to the predetermined isothermal temperatures T_c ranged from 113 to 130 °C. The crystallization time was taken as the sample temperature reaches the prefixed T_c and the development of exothermic heat flow was recorded until the measurable crystallization of the materials was complete.

5.1.3 Isothermal crystallization morphology by POM

The growth of crystalline structure for PLA and its composites during isothermal crystallization process was monitored using polarized optical microscope (Leica, DMLP HC) equipped with an automated hot-stage (Mettler Toledo, FP82HT). About 5.0 ± 0.2

mg of individual specimens were sandwiched between two microscope cover slides, melted at 180 °C, and vertically pressed with slight force to form thin films. The films were annealed for 10 min to remove the thermal effect and the preexisting PLA crystallites. After that, they were rapidly cooled down to 130 °C at a rate of 20 °C/min, and eventually allowed to crystallize under isothermal condition. The optical photographs of crystalline morphology were taken as a function of crystallization time.

5.2 Results and discussion

5.2.1 Kinetics of isothermal crystallization by Avrami model

The effect of morphology of PBT on the isothermal crystallization kinetics of neat PLA and the PLA/PBT composites are analyzed by DSC at crystallization temperatures ranging between 113-130 °C. Figure 5.1 depicts the DSC thermograms of neat PLA, SP-M and FIBER-M at various isothermal crystallization temperatures. For brevity, it is noteworthy that the crystallization of neat PLA takes too much time for completing the DSC measurement when the temperature over 120 °C (longer than 2 h) and thus the DSC traces between 113-120 °C are examined. The exothermic heat flow is developed at the early stage, which is indicative of the beginning of nucleation. The heat flow gradually increases reaching the maximum and decreases afterwards due to the collision of adjacent PLA crystals which impedes the growth process. Eventually, the heat flow returns to the baseline suggesting a complete crystallization.

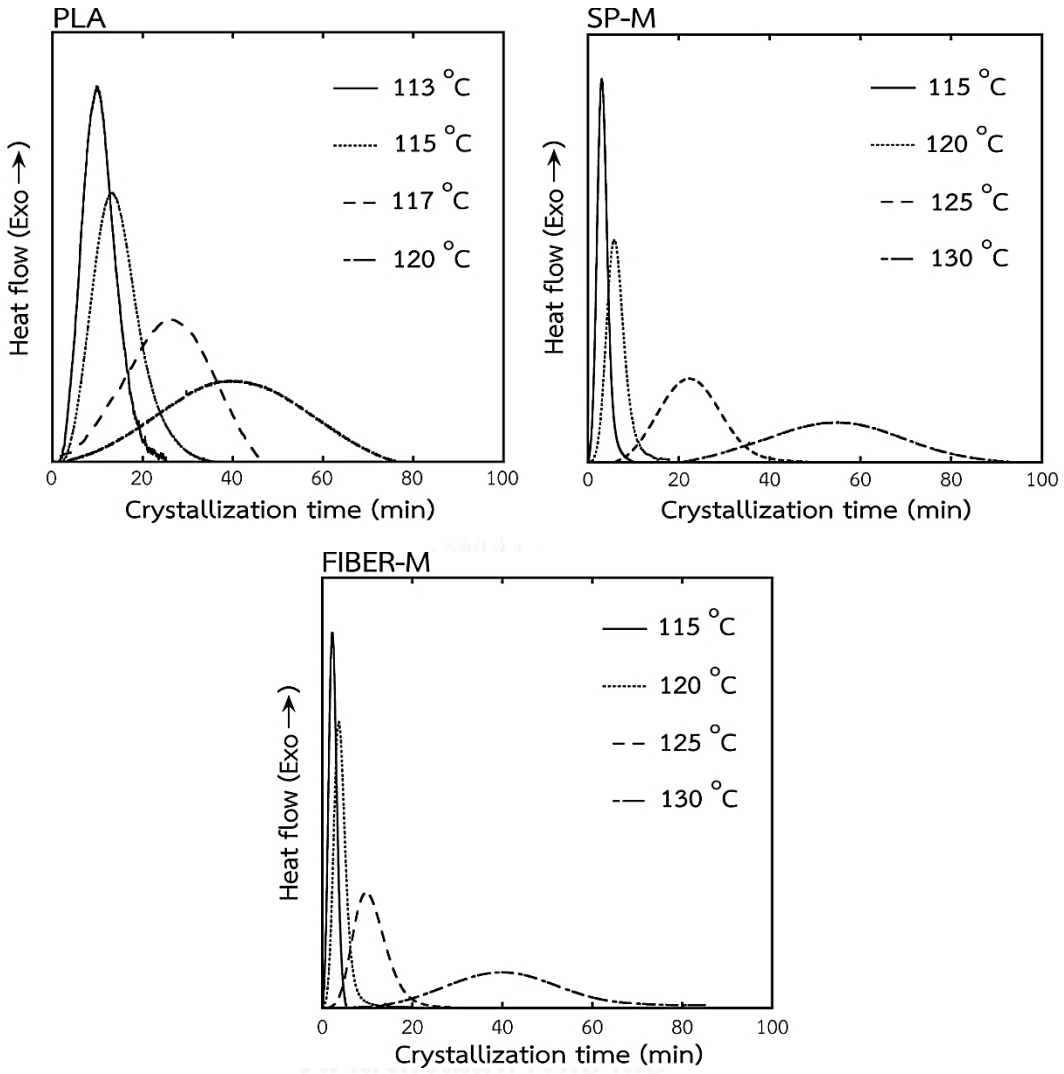

Figure 5.1 DSC thermograms of isothermal crystallization for neat PLA, SP-M and FIBER-M at various isothermal crystallization temperatures

As can be seen in the figures, the overall crystallization time is lengthened and the crystallization peaks become broader significantly as the isothermal crystallization temperature T_c increases in this range of studied temperatures, as expected on the basis of fundamental nucleation theory in which a reduction in a number of nuclei

interferes the crystallization growth in spite of higher mobility of polymer chains [96]. A lag of a development of heat flow after the sample temperature reaches the desired T_c, where $t = 0$, is obvious for SP-M and FIBER-M at T_c = 130 °C, which reflects a slow induction of crystallization. At isothermal crystallization temperature of 120 °C, the values of the maximum crystallization time t_{max} for neat PLA, SP-M and FIBER-M are 39.23, 5.83 and 3.67 min, respectively, pointing out that PBT can effectively accelerate the crystallization rate of PLA.

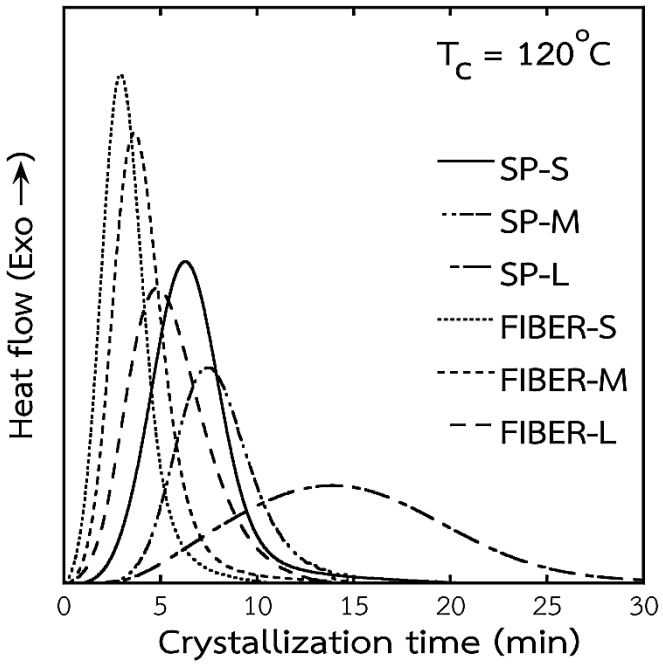

Figure 5.2 DSC thermograms of isothermal crystallization for PLA/PBT composites at 120 °C

The DSC thermograms of the PLA/PBT composites at isothermal crystallization temperature of 120 °C are demonstrated in Figure 5.2. This temperature is chosen because it is high enough to clarify the nucleating effect of PBT on the crystallization of PLA in an appropriate window of over crystallization time. Further, the plot of PLA is omitted since PLA crystallize very slow and adding it to the graph makes the more difficulty to analyze. The crystallization isotherms for the other conditions show very similar trends and, thus, are not presented. The values of t_{max} for samples at 120 °C increase in the following order: FIBER-S, FIBER-M, FIBER-L, SP-S, SP-M, and SP-L. Considering only the composites containing the same type of PBT dispersion, t_{max} value is monotonically shortened as the size of dispersed phase declines because smaller particles have larger specific surface area which acts as the nucleation site for PLA to nucleate and accordingly grow. By knowing the final composition and the average size of the dispersed PBT, the approximate specific surface area of spherical and fibrous PBT domains in the composites can be calculated as follows: 0.19 m^2/g for SP-S, 0.10 m^2/g for SP-M, 0.04 m^2/g for SP-L, 0.67 m^2/g for FIBER-S, 0.26 m^2/g for FIBER-M, and 0.08 m^2/g for FIBER-L. Consequently, the large specific surface area of FIBER-S is responsible for fast crystallization rate, which is in agreement with the investigation done by Kose and Kondo [71].

Interestingly, FIBER-L exhibits faster crystallization rate than SP-S in spite of the fact that FIBER-L has less specific surface area, which is about one-half that of SP-S. This result indicates that the specific surface area is not the only factor that influences

the crystallization rate of PLA in our study. Hence, a theoretical Avrami model is conducted to investigate the crystallization kinetics of the PLA/PBT composites.

The Avrami equation [97] is widely used in order to obtain relevant parameters for characterizing the isothermal crystallization kinetics of polymers and its general form is given as follows:

$$1 - X_c(t) = \exp(-kt^n)$$

By taking a double logarithm of equation (5), the Avrami equation is converted into a general linear form:

$$\log\left[-\ln\left(1 - X_c(t)\right)\right] = \log(k) + n\log(t)$$

where $X_c(t)$ is time-dependent relative volumetric crystallinity, k is the temperature-dependent crystallization rate constant which characterizes the rate of nucleation and growth, and n is Avrami index (Avrami exponent) containing the information on nucleation and growth geometry of the crystallizable material. The degree of crystallinity $X_c(t)$ can be calculated with the following equation.

$$X_c = \frac{X_c(t)}{X_c(t=\infty)} = \frac{\int_0^t \frac{dH(t)}{dt} dt}{\int_0^\infty \frac{dH(t)}{dt} dt}$$

where $H(t)$ is a heat flow obtained from the isothermal DSC traces and $X_c(t)$ is the ratio of exothermic area at elapsed crystallization time t to the total area until the crystallization ends.

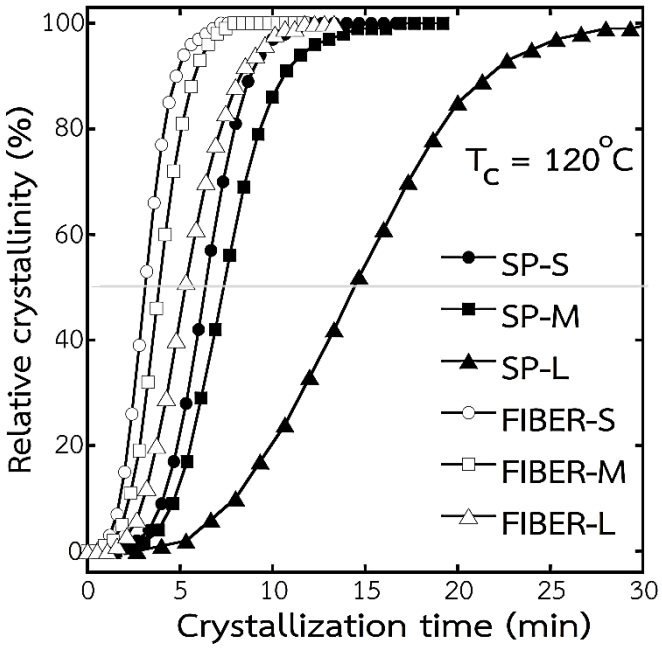

Figure 5.3 Development of relative degree of crystallinity X_c versus crystallization time t for PLA/PBT composites at 120 °C. The inserted horizontal line is X_c = 50%

Figure 5.3 illustrates the relative degree of crystallinity X_c versus crystallization time t for the composites at 120 °C. The curve slowly increases at the beginning as a result of formation of primary nuclei and then shows a straight line, indicating that the growth rate of PLA crystallites is a constant and does not depend on the extent of crystallinity. Because Avrami equation rarely explains the crystallization behavior of polymer the whole conversion, choosing the range of conversion is of importance to provide the reliable and satisfactory information. Namely, the initial data points (X_c < 3%) and aftermost data points (X_c > 80%) should not be considered because of the

experimental errors owing to the unsteady DSC detection due to small amount of heat developed and the secondary crystallization process, respectively [98].

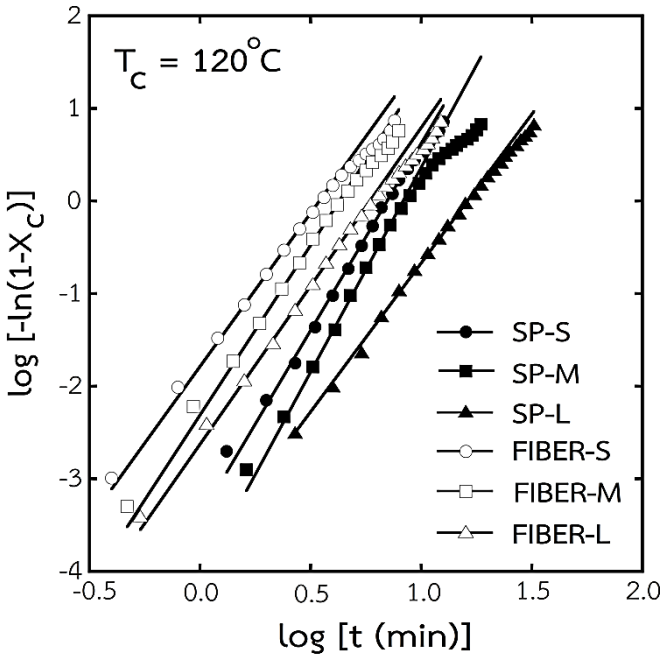

Figure 5.4 Avrami plots of log[-ln(1- X_c)] versus log t for isothermal crystallization of neat PLA and its composite at 120 °C (symbols: experimental data; solid lines: linear fitting by Avrami model).

Figure 5.4 displays the graphs plotting log[-ln(1- X_c)] against log(t) according to equation (3) for neat PLA and its composites. The solid lines represent the fitted data using Avrami model, meanwhile the symbols are the experimental data. The Avrami index n values and the crystallization rate constant k values can be yielded from the slope and the y-intercept of the curves, respectively. It is found that the straight lines

from Avrami model fitted the experimental data with large coefficient of determination (R^2 > 99%) in the relative degree of crystallinity of crystallizing polymer between 5% and 50%, suggesting that the Avrami equation is valid for explaining the isothermal crystallization mechanism of the PLA/PBT composites in this selected conversion range. Moreover, the marked deviation of the experimental values from the Avrami linearity is noticed at the later stage of crystallization process, which can be primarily ascribed to the occurrence of secondary crystallization phenomena due to the impingement of spherulites at long crystallization time [99].

Another important Avrami parameter is crystallization half-time $t_{1/2}$, which is defined as the time required for polymer to complete half of the total degree of crystallinity, and can be calculated as expressed with the following equation;

$$t_{1/2} = (\ln 2/k)^{1/n}$$

where *k* and *n* are acquired from the Avrami equation fitted in Figure 5.4. The bulk crystallization rate is analyzed by this crystallization half-time. Figure 5.5 illustrates the plot of $t_{1/2}$ versus T_c for neat PLA and its composites. Virgin PLA has prolonged $t_{1/2}$ with respect to the composites, demonstrating that PBT has nucleating effect for improving crystallization rate of PLA. At low crystallization temperature, *i.e.*, 115 °C, $t_{1/2}$ of all composites are insignificantly different. On the contrary, the composites containing fibrous dispersion exhibit considerably shorter $t_{1/2}$ than those containing spherical

dispersion at high T_c, which is elucidated that fibrous dispersion is more capable for facilitating crystallization in comparison with spherical dispersion.

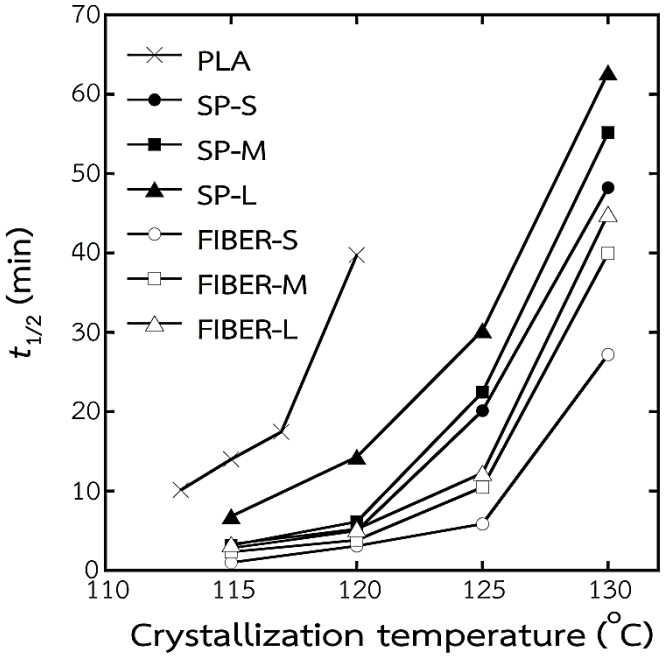

Figure 5.5 Isothermal crystallization half-time $t_{1/2}$ as a function of isothermal crystallization temperature for neat PLA and its composites.

Table 5.1 lists the Avrami parameters under isothermal crystallization including Avrami index n, overall crystallization rate constant k, maximum crystallization time t_{max}, and crystallization half-time $t_{1/2}$. These kinetic parameters are very sensitive to the crystallization temperature. Namely, k value decreases and $t_{1/2}$ increases value with increasing T_c because the intense thermal motion of polymer segments retards the formation of nuclei and growth process. For examples: increasing T_c of FIBER-S from

115 to 120, 125 and 130 °C decreases *k* values from 1.80 × 10^{-1} to 1.62 × 10^{-2}, 1.09 × 10^{-3} and 2.70 × 10^{-6} min^{-1}, respectively. The values of *k* and $t_{1/2}$ for neat PLA are lower and longer than those of composites, especially FIBER-S, respectively; mentioning that large specific surface area of PBT is favorable as nucleating agent for increasing crystallization rate of PLA. An increase in *k* value owing to the incorporation of PBT in PLA matrix is responsible for an enhancement of overall isothermal crystallization rate. The average *n* values for all samples are close in a range from 3.4 to 4, referring that introducing PBT in the PLA composites does not obviously influence the nucleation pattern and nucleation mechanism, and the crystallization mode is the three-dimensional crystallization growth dominantly initiated by homogeneous nucleation in a temperature range explored here [100-102].

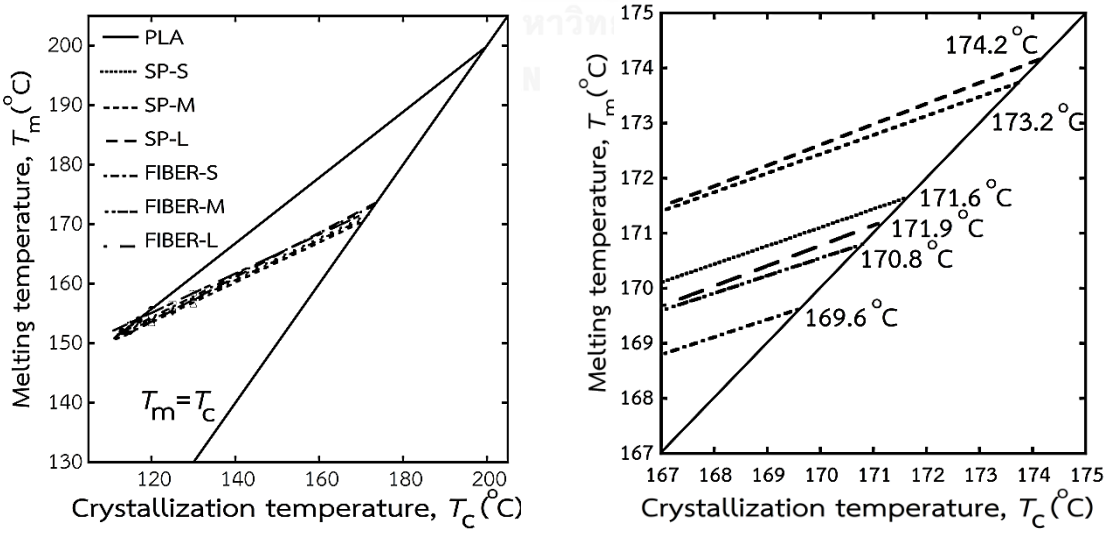

Figure 5.6 Melting temperature T_m of PLA as a function of isothermal crystallization temperature T_c for neat PLA and its composites

Table 5.1 Isothermal crystallization kinetic parameters calculated from Avrami model for neat PLA and its composites at different crystallization temperatures

Sample	T_c (°C)	Avrami index n	k (min^{-n})	$t_{1/2}$ (min)	t_{max} (min)	R^2
Neat PLA	113	3.44	1.08×10^{-4}	10.16	9.73	0.9998
	115	3.53	6.77×10^{-5}	14.00	13.50	0.9996
	117	3.66	2.72×10^{-6}	17.45	15.98	0.9986
	120	3.89	1.62×10^{-7}	39.76	39.23	0.9971
SP-S	115	3.63	1.60×10^{-2}	2.82	2.73	0.9999
	120	4.17	8.44×10^{-4}	5.00	6.32	0.9997
	125	3.88	6.05×10^{-6}	20.13	20.70	0.9998
	130	3.83	2.47×10^{-7}	48.26	49.13	0.9999
SP-M	115	3.42	1.36×10^{-2}	3.16	3.05	0.9999
	120	4.32	2.73×10^{-4}	6.14	5.83	0.9989
	125	4.09	2.06×10^{-6}	22.46	22.30	0.9997
	130	4.12	4.62×10^{-8}	55.18	55.08	0.9998
SP-L	115	3.02	2.11×10^{-3}	6.81	6.27	0.9995
	120	3.21	1.36×10^{-4}	14.29	13.87	0.9992
	125	3.29	9.34×10^{-6}	30.23	30.77	0.9998
	130	3.85	8.32×10^{-8}	62.75	61.98	0.9999
FIBER-S	115	2.83	1.80×10^{-1}	1.61	1.30	0.9972
	120	3.32	1.62×10^{-2}	3.10	2.93	0.9999
	125	3.65	1.09×10^{-3}	5.86	5.67	0.9995
	130	3.77	2.70×10^{-6}	27.22	27.43	0.9992
FIBER-M	115	2.98	5.47×10^{-2}	2.34	2.18	0.9999
	120	3.71	4.76×10^{-3}	3.83	3.67	0.9998
	125	3.84	8.34×10^{-5}	10.49	9.72	0.9982
	130	3.89	4.07×10^{-7}	39.98	39.80	0.9999
FIBER-L	115	2.81	2.39×10^{-2}	3.31	3.02	0.9996
	120	3.47	2.26×10^{-3}	5.21	4.85	0.9997
	125	3.79	5.14×10^{-5}	12.29	11.57	0.9985
	130	3.95	2.66×10^{-7}	44.92	47.63	0.9999

The DSC melting endotherms for all examined samples isothermally crystallized at T_c ranged 113-130 °C reveal the single melting peak of PLA around 152-159 °C and, in addition, T_m increases as a function of T_c. According to the Hoffman-Weeks theory [103], the equilibrium melting temperature $\boldsymbol{T_m^0}$ is an intersection of T_m versus T_c plots linearly extrapolating to the lines of $T_m = T_c$, as depicted in Figure 5.6. It is found that $\boldsymbol{T_m^0}$ for neat PLA is about 199.8 °C which is close to the value reported by Tsuji and Miyauchi [104], whereas the $\boldsymbol{T_m^0}$ for the PLA/PBT composites is reduced in a range from 170 to 174 °C, indicating about 30 °C melting point depression. It could be understood that PBT markedly decreases the perfectness and finite size of PLA crystals, leading to an inhibition of isothermal thickening of PLA lamellar crystals and therefore depressed equilibrium melting temperature.

5.2.2 Observation of development of crystalline structure of PLA under isothermal condition

The development of crystalline morphology for neat PLA and its composites during isothermal crystallization at 130 °C is monitored using a polarized optical microscope (POM) as illustrated in Figure 5.7. This temperature is selected because it allows the clear observation on the nucleation and growth rates of PLA in the composites. The bright spots in the POM images before the crystallization begins (t = 0 min) are the crystalline PBT dispersed domains in the PLA matrix. As can be seen,

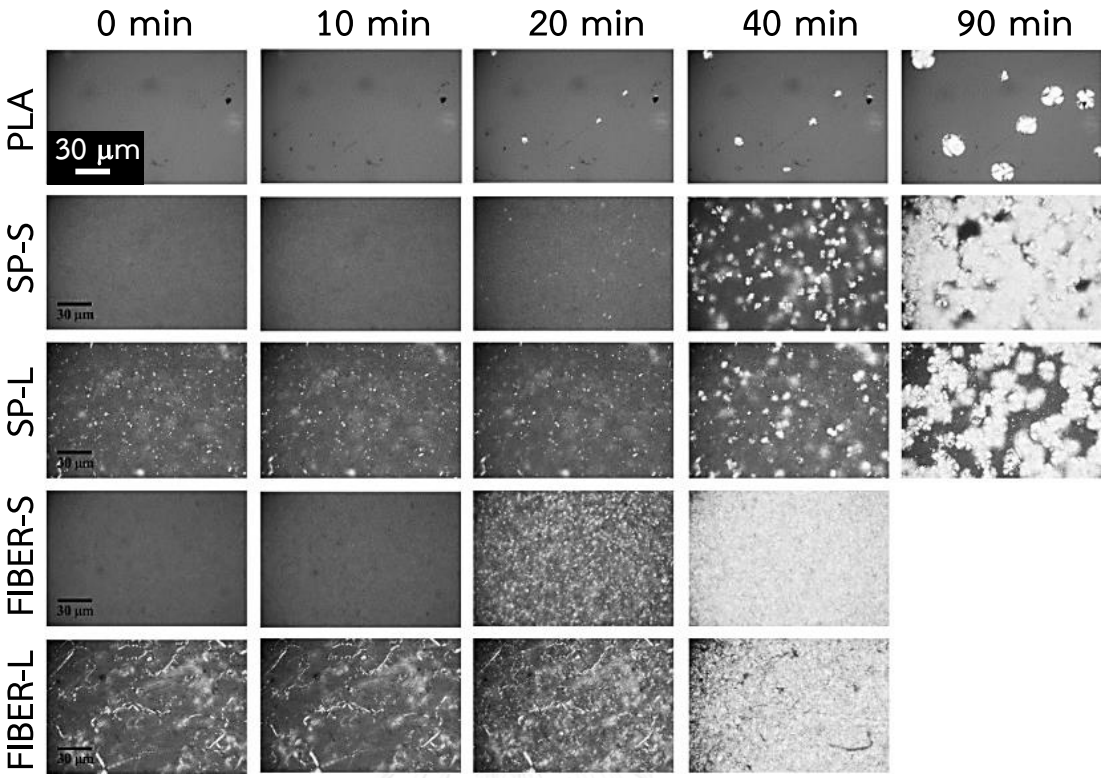

Figure 5.7 Polarized optical images for neat PLA and its composites under the crossed polars after an isothermal crystallization from the melt (T_c = 130 °C)

pure PLA gradually crystallizes from the melt at this temperature after 20 min and the PLA crystals grow in outward direction, resulting in the distinctive and relatively large spherulites with a well-developed Maltese cross after a long crystallization time. For the composites, PBT particles acting as additional nucleating sites fasten the crystallization rate of PLA by increasing the nucleation density, thus the spherulitic crystals quickly impinge upon each other leading to a formation of dense finer spherulites comparing with neat PLA owing to the space confinement for each nucleus.

Considering the composites comprising the same shape of PBT, the number of nucleating sites increases and the rate of crystal nuclei formation is facilitated as the size of PBT reduces because of larger specific surface area, corresponding to the isothermal DSC studies. The crystallization rate is more pronounced for the composites containing fibrous dispersion of PBT, particularly Fiber-S, further demonstrating that fibrous particles can prominently accelerate the nucleating rate of PLA with respect to spherical particles probably because the nucleation rate of crystalline of PLA around the fibers relatively is faster than that in the bulk [105]. This implies that type of PBT dispersion also plays an important role in crystallization rate of PLA.

CHAPTER VI

CONCLUSIONS AND RECOMMENDATION

6.1 Overall conclusions

In brief, this dissertation focused not only on preparing the PLA/PBT microporous films by biaxial stretching technique, but also improving the thermal properties of the PLA composites by incorporation of PBT. The effects of morphologies, *i.e.*, shape and size, of PBT on the properties of unstretched PLA composites and PLA biaxially stretched films are comparatively investigated.

First of all, we have proposed the methodology to achieve the PLA composites containing different sizes and shapes of PBT irrespective of influence of composition by controlling the composition, mixing temperature and mixing protocol. The considerably long PBT fibers in the composites are obtained by using capillary rheometer at high shear rate as confirmed by SEM data. Moreover, the rheological and tensile characterizations imply the random network structure of interdigitated PBT fibers formed upon kneading. DMA and DSC analysis indicates an improvement of cold crystallization and crystallization of PLA owing to the presence of PBT particles.

For the PLA/PBT biaxially stretched films, the PBT dispersed domains theoretically act as stress concentrator, accumulating the stress around the dispersed

domains especially at polar region, and the stress inside the specimen overcomes the interfacial adhesion between PLA matrix and PBT particles, resulting in the void opening phenomenon. For the stretched films composed of spherical dispersion, the void size notably relates to the size of PBT droplet because the ability of stress concentrator increases as the particle size becomes larger. However, the void content is insignificantly different as the size of PBT droplet increases, which can be explained as the SP-S gives a lot of small voids, while the SP-L has a small amount of larger voids. For the stretched films comprising fibrous dispersion, the films show the affine deformation as can be seen by a remarkably increase in stress during film stretching. Moreover, the localized deformation between PBT fibers is expected to be the original of void opening. FIBER-L shows the highest void content of about 8%. Additionally, the stretched films exhibit improved crystallinity and reduced enthalpy of cold crystallization as a result of strain-induced crystallization, particularly at high stretching ratio. In addition, FIBER-L films biaxially stretched at $\lambda_x \times \lambda_y = 3 \times 3$ show the highest WVP value of 1038.53 gm.mil/m^2.day.

Finally, the effect of PBT morphology on the isothermal crystallization behavior of PLA matrix is reported. PBT accelerates the crystallization rate of PLA as evidenced by the shortened crystallization half-time $t_{1/2}$ and high overall crystallization rate constant k. It is found that the crystallization rate strongly depends on the specific surface area of dispersed PBT domains. The Avrami index n of all samples is lied

between 3-4, suggesting that PBT does not affect the nucleation mechanism; however, the depression of equilibrium melting temperature in the composites ascribes the reduced perfectness and size of crystalline of PLA. Besides, it is expected that the nucleation rate of PLA around PBT fiber is faster than that in the bulk, which implies that type of PBT dispersion also plays a key role in the crystallization of PLA.

6.2 Recommendations

- Owing to the limitation of biaxial stretching machine, the stretched films are small which restricts to measure some important properties of the films including gas permeation, tensile properties, tear strength, impact strength. Thus, the instrument that can create larger stretched films is important.

- Instead of measuring the difference in apparent bulk density of specimen for calculation of void content, more precise technique should be also conducted to examine porous structure such as gas adsorption using Brunauer-Emmett-Teller (BET) equation.

- The polymer chain orientation in the stretched films should be also measured.

- Effects of PBT content on the properties of the composites and porous structure of the stretched films should be investigated.

REFERENCES

[1] Department of International Trade Promotion. สินค้าผัก ผลไม้สด แช่เย็นและแห้ง. [Online]. 2014. Available from: http://www.ditp.go.th/contents_attach/85805/85805.pdf [2014, October 12]

[2] Jamjumroon, S. et al. Extending the shelf-life of straw muchroom with high carbon dixoide treatment. **J. Food Agric. Environ.** 10 (2012): 78-84.

[3] Luengwilai, K., Backles, D.M., Plumjit, O., and Siriphanich, J. Postharvest quality and storage life of 'Makapuno' coconut (Cocos nucifera L.). **Sci. Hort.** 175 (2014): 105-110.

[4] Yimyong, W., and Soni, P. Effects of modified atmosphere packaging on quality of cut Dendrobium orchid. **J. Food Agric. Environ.** 12 (2014): 408-411.

[5] Rouquerol, J. et al. Recommendations for the characterization of porous solids. **Pure & Appl. Chem.** 66 (1994): 1739-1758.

[6] Loeb, S., and Sourirajan, S. High flow porous membranes for separating water from saline solutions **U.S. Patent, 3,133,132 A**, 1964.

[7] Khulbe, K.C., Feng, C.Y., and Matsuura, T. Synthetic polymeric membranes: Characterization by Atomic Force Microscopy. **Springer**: Heidelberg, 2008.

[8] Gao, L., Tang, B., and Wu, P. An experimental investigation of evaporation time and the relative humidity on a novel positively charged ultrafiltration membrane via dry-wet inversion. **J. Membr. Sci.** 326 (2009): 168-177.

[9] Madaeni, S.S., and Moradi, P. Preparation and characterization of asymmetric polysulfone membrane for separation of oxygen and nitrogen gases. **J. Appl. Polym. Sci.** 121 (2011): 2157-2167.

[10] Yoon, J., Lesser, A.J., and McCarthy, T.J. Locally anisotropic porous materials from polyethylene and crystallizable diluents. **Macromolecules** 42 (2009): 8827-8834.

[11] Zhang, H. et al. High density polyethylene-grafted-maleic anhydride low-*k* porous films prepared via thermally induced phase separation. **Eur. Polym. J.** 44 (2008): 1095-1101.

[12] Sa-nguanruksa, J., Rujiravanit, R., Suphol, P., and Tokura, S. Porous polyethylene membranes by template-leaching technique: Preparation and characterization. **Polym. Test.** 23 (2004): 91-99.

[13] Riscanu, D., Favis, B.D., Feng, C., and Matsuura, T. Thin-film membranes derived from co-continuous polymer blends: Preparation and performance. **Polymer** 45 (2004): 5597-5609.

[14] González-Buesa, J., Ferrer-Mairal, A., Oria, R., and Salvador, M.L. Alternative method for determining O_2 and CO_2 transmission rates through microperforated films for modified atmosphere packs. **Packag. Technol. Sci.** 26 (2013): 413-421.

[15] Winotapun, C., Kerddofag, N., and Chinsirikul, W. Nd:YAG laser perforation of plastic films for enhanced breathability. **Adv. Mat. Res.** 93-94 (2010): 79-82.

[16] Bierenbaum, H.S., Isaacson, R.B., and Lantos, P.R. Breathable medical dressing **U.S. Patent, 3,426,754**, 1969.

[17] Arora, P., and Zhang, Z. Battery separators. **Chem. Rev.** 104 (2004): 4419-4462.

[18] Gore, R.W. Process for producing porous products **U.S. Patent, 3,953,566**, 1976.

[19] Kremer, F., and Schönhals, A. Broad dielectric spectroscopy. **Springer**: Heidelberg, 2003.

[20] Sadeghi, F., Ajji, A., and Carreau, P.J. Analysis of microporous membranes obtained from polypropylene films by stretching. **J. Membr. Sci.** 292 (2007): 62-71.

[21] Sadeghi, F., Tabatabaei, S.H., Ajji, A., and Carreau, P.J. Effect of PVDF characteristics on extruded film morphology and porous membranes feasibility by stretching. **J. Polym. Sci.** 47 (2009): 1219-1229.

[22] Zhu, W. et al. A novel polypropylene microporous film. **Polym. Adv. Technol.** 7 (1996): 743-748.

[23] Zuo, F. et al. The role of interlamellar chain entanglement in deformation-induced structure changes during uniaxial stretching of isotactic polypropylene. **Polymer** 48 (2007): 6867-6880.

[24] Chandavasu, C., Xanthos, M., Sirkar, K.K., and Gogos, C.G. Fabrication of microporous polymeric membranes by melt processing of immiscible blends. **J. Membr. Sci.** 211 (2003): 167-175.

[25] Liu, M., Xiao, C., and Hu, X. Optimization of polyurethane-based hollow fiber membranes morphology and performance by post-treatment methods. **Desalination** 275 (2011): 133-140.

[26] Auras, R., Harte, B., and Selke, S. An overview of polylactides as packaging materials. **Macromol. Biosci.** 4 (2004): 835-864.

[27] Drumright, R.E., Gruber, P.R., and Henton, D.E. Polylactic acid technology. **Adv. Mater.** 12 (2000): 1841-1846.

[28] Okamoto, M., and B., J. Synthetic biopolymer nanocomposites for tissue engineering scaffolds. **Prog. Polym. Sci.** 38 (2013): 1487-1503.

[29] Serra, T., Planell, J.A., and Navarro, M. High-resolution PLA-based composite scaffolds via 3-D printing technology. **Acta Biomater.** 9 (2013): 5521-5530.

[30] Arrieta, M.P., López, J., Hernández, A., and Rayón, E. Ternary PLA-PHB-Limonene blends intended for biodegradable food packaging applications. **Eur. Polym. J.** 50 (2014): 255-270.

[31] Gonçalves, C.M.B. et al. Effect of natural and synthetic antioxidants incorporation on the gas permeation properties of poly(lactic acid) films. **J. Food Eng.** 116 (2013): 562-571.

[32] Siracusa, V. et al. Poly(lactic acid)-modified films for food packaging application: Physical, mechanical, and barrier behavior. **J. Appl. Polym. Sci.** 125 (2012): E390-E401.

[33] Auras, R.A., Lim, L.T., Selke, S.E.M., and Tsuji, H. Poly(lactic acid): Synthesis, Structures, Properties, Processing, and Applications. **John Wiley & Sons**: New Jersey, 2011.

[34] Jiamjitsiripong, K., and Pattamaprom, C. Effects of epoxidized natural rubber on gas barrier and mechanical properties of NR/BIIR composites. **J. Elastomers Plast.** 43 (2011): 341-355.

[35] Sabzi, M., Jiang, L., Liu, F., Ghasemi, I., and Atai, M. Graphene nanoplatelets as poly(lactic acid) modifier: linear rheological behavior and electrical conductivity. **J. Mater. Chem. A** 1 (2013): 8253-8261.

[36] Li, Y., Chen, C., Li, J., and Sun, X.S. Isothermal crystallization and melting behaviors of bionanocomposites from poly(lactic acid) and TiO_2 nanowires. **J. Appl. Polym. Sci.** 124 (2012): 2968-2977.

[37] Najafi, N., Heuzey, M.C., and Carreau, P.J. Crystallization behavior and morphology of polylactide and PLA/clay nanocomposites in the presence of chain extenders. **Polym. Eng. Sci.** 53 (2013): 1053-1064.

[38] Acar, I., Durmuş, A., and Özgümüş, S. Nonisothermal crystallization kinetics and morphology of polyethylene terephthalate modified with polylactic acid. **J. Appl. Polym. Sci.** 106 (2007): 4180-4191.

[39] Yokohara, T., and Yamaguchi, M. Structure and properties for biomass-based polyester blends of PLA and PBS. **Eur. Polym. J.** 44 (2008): 677-685.

[40] Jiang, L., Wolcott, M.P., and Zhang, J. Study of biodegradable polylactide/poly(butylene adipate-co-terephthalate) blends. **Biomacromolecules** 7 (2006): 199-207.

[41] Ali, M.A.B.M., Nobukawa, S., and Yamaguchi, M. Morphology development of polytetrafluoroethylene in a polypropylene melt (IUPAC Technical Report). **Pure. Appl. Chem.** 83 (2011): 1819-1830.

[42] Ali, M.A.B.M., Okamoto, K., Yamaguchi, M., Kasai, T., and Koshirai, A. Rheological properties for polypropylene modified by polytetrafluoroethylene. **J. Polym. Sci., Part B: Polym. Phys.** 47 (2009): 2008-2014.

[43] Yamaguchi, M., Fukuda, K., Yokohara, T., Amran, M., and Nobukawa, S. Modification of rheological properties under elongational flow by addition of polymeric fine fibers. **Macrol. Mater. Eng.** 297 (2012): 654-658.

[44] Yokohara, T., Nobukawa, S., and Yamaguchi, M. Rheological proeprties of polymer composites with flexible fine fibers. **J. Rheol.** 55 (2011): 1205-1218.

[45] Migler, K.B. String formation in sheared polymer blends: coalescence, breakup, and finite size effects. **Phys. Rev. Lett.** 86 (2001): 1023-1026.

[46] Chandavasu, C., Xanthos, M., Sirkar, K.K., and Gogos, C.G. Polypropylene blends with potential as materials for microporous membranes formed by melt processing. **Polymer** 43 (2002): 781-795.

[47] Chandavasu, C., Xanthos, M., Sirkar, K.K., and Gogos, C.G. Preparation of microporous films from immiscible blends via melt processing. **J. Plast. Film Sheeting** 16 (2000): 288-300.

[48] Park, J.-S., Gwon, S.-J., Lim, Y.-M., and Nho, Y.-C. Influence of the stretching temperature on an alumina filled microporous high density polyethylene membrane. **Mater. Des.** 31 (2001): 3215-3219.

[49] Qaiss, A., Saidi, H., Fassi-Fehri, O., and Bousmina, M. Porosity formation by biaxial stretching in polyolefin films filled with calcium carbonate particles. **J. Appl. Polym. Sci.** 123 (2012): 3425-3436.

[50] Shields, R.J., Bhattacharyya, D., and Fakirov, S. Fibrillar polymer-polymer composites: Morphology, properties and applications. **J. Mater. Sci.** 43 (2008): 6758-6770.

[51] Cassagnau, P., and Michel, A. New morphologies in immiscible polymer blends generated by a dynamic quencing process. **Polymer** 42 (2001): 3139-3152.

[52] Manas-Zloczower, I. Mixing and Compounding of Polymers. **Hanser**: Munich, 2009.

[53] Boyaud, M.F., Cassagnau, P., Michel, A., Bousmina, M., and Ait-Kadi, A. Transient elongational properties of an in situ generated polymer/polymer composite. **Polym. Eng. Sci.** 41 (2001): 684-695.

[54] Hong, J.S., Ahn, K.H., and Lee, S.J. Strain hardening behavior of polymer blends with fibril morphology. **Rheol. Acta.** 45 (2005): 202-208.

[55] Monticciolo, A., Cassagnau, P., and Michel, A. Fibrillar morphology development of PE/PBT blends: Rheology and solvent permeability. **Polym. Eng. Sci.** 38 (1998): 1882-1889.

[56] Takahashi, T., Takimoto, J., and Koyama, K. Uniaxial elongational viscosity of various molten polymer composites. **Polym. Compos.** 20 (1999): 357-366.

[57] Yokohara, T., Okamoto, K., and Yamaguchi, M. Effect of the shape of dispersed particles on the thermal and mechanical properties of biomass polymer blends composed of poly(L-lactide) and poly(butylene succinate). **J. Appl. Polym. Sci.** 117 (2010): 2226-2232.

[58] Yamaguchi, M., Fukuda, K., Yokohara, T., Amran, M., and Nobukawa, S. Modification of rheological properties under elongational flow by addition of polymeric fine fibers. **Macromol. Mater. Eng.** 297 (2012): 654-658.

[59] Mewis, J., and Metzner, A.B. The rheological properties of suspensions of fibers in Newtonian fluids subjected to extensional deformations. **J. Fluid Mech.** 62 (1974): 593-600.

[60] Bouaziz, A., Zaïri, F., Naït-Abdelaziz, M., Gloaguen, J.M., and Lefebrve, J.M. Micromechanical modelling and experimental investigation of random discontinuous glass fiber polymer-matrix composites. **Compos. Sci. Technol.** 67 (2007): 3278-3285.

[61] Houshyar, S., and Shanks, R.A. Tensile properties and creep response of polypropylene fibre composites with variation of fibre diameter. **Polym. Int.** 53 (2004): 1752-1759.

[62] Noda, K., Takahara, A., and Kajiyama, T. Fatique failure mechanisms of short glass-fiber reinforced nylon 66 based on nonlinear dynamic viscoelastic measurement. **Polymer** 42 (2001): 5803-5811.

[63] Menczel, J., and Varga, J. Influence of nucleating agents on crystallization of polypropylene. **J. Therm. Anal.** 28 (1983): 161-174.

[64] Lepers, J.C., Favis, B.D., and Kent, S.L. Interface-property relationships in biaxially stretched PP-PET blends. **Polymer** 41 (2000): 1937-1946.

[65] Wu, S. Formation of dispersed phase in incompatible polymer blends: Interfacial and rheological effects. **Polym. Eng. Sci.** 27 (1987): 335-343.

[66] Ji, X.L., Jing, J.K., and Jiang, B.Z. Tensile modulus of polymer nanocomposites. **Polym. Eng. Sci.** 42 (2002): 983-993.

[67] Lazzeri, A., Thio, Y.S., and Cohen, R.E. Volume strain measurements on $CaCO_3$/polypropylene particulate composites: The effect of particle size. **J. Appl. Polym. Sci.** 91 (2004): 925-935.

[68] Mishra, S., Sonawane, S.H., and Singh, R.P. Studies on characterization of nano $CaCO_3$ prepared by in situ deposition technique and its application in PP-nano $CaCO_3$ composites. **J. Polym. Sci., Part B: Polym. Phys.** 43 (2005): 107-113.

[69] Singh, R.P., Zhang, M., and Chan, D. Toughening of a brittle thermosetting polymer: Effects of reinforcement particle size and volume fraction. **J. Mater. Sci.** 37 (2002): 781-788.

[70] Wang, Y., Tong, B., Hou, S., Li, M., and Shen, C. Transcrystallization behavior at the poly(lactic acid)/sisal fibre biocomposite interface. **Composites Part A** 42 (2011): 66-74.

[71] Kose, R., and Kondo, T. Size effects of cellulose nanofibers for enhancing crystallization of poly(lactic acid). **J. Appl. Polym. Sci.** 128 (2013): 1200-1205.

[72] Wu, P.C., Jones, G., Shelley, C., and Woelfli, B. Novel microporous films and their composites. **J. Eng. Fibers Fabr.** 2 (2007): 49-59.

[73] Steffe, J.F. Rheological Methods in Food Process Engineering. **Freeman Press**: Michigan, 1996.

[74] Ou, X., and Cakmak, M. Influence of biaxial stretching mode on the crystalline texture in polylactic acid films. **Polymer** 49 (2008): 5344-5352.

[75] Ou, X., and Cakmak, M. Comparative study on development of structural hierarchy in constrained annealed simultaneous and sequential biaxially stretched polylactic acid films. **Polymer** 51 (2010): 783-792.

[76] Delpouve, N., Stoclet, G., Saiter, A., Dargent, E., and Marais, S. Water barrier properties in biaxially drawn poly(lactic acid) films. **J. Phys. Chem. B** 116 (2012): 4615-4625.

[77] Tsai, C.-C. et al. Crystallinity and dimensional stability of biaxial oriented poly(lactic acid) films. **Polym. Degrad. Stab.** 95 (2010): 1292-1298.

[78] Zhang, X. et al. Structure variation of tensile-deformed amorphous poly(L-lactic acid): Effects of deformation rate and strain. **Polymer** 52 (2011): 4141-4149.

APPENDICES

APPENDIX A

CALCULATION FOR THE PLA/PBT COMPOSITES

The calculation of SP-L is shown as an example as demonstrated below. However, other composites can also be calculated in the similar steps.

Detail: preparation of PLA/PBT (95/5 v/v) from PLA/PBT composites (60/40 v/v)

Important information:

Density of PLA	1.24	g/cm^3
Density of PBT	1.30	g/cm^3
Capacity of internal batch mixer	60	cm^3
Fill factor	70	%
Final composition of PLA/PBT composites	95/5	v/v
Content of thermal stabilizer	5000	ppm

Step 1 Calculation of total volume of composites in the internal batch mixer

Volume of composites = (Volume of internal batch mixer) × (Fill factor)

$= 60 \times 0.7 = 42$ cm^3

Step 2 Preparation of the composites (60/40)

Weight of each polymer = (Volume of composites) × (Volume fraction) × (Density)

PLA = (42 cm^3 composites) × (60/100) × (1.24 g/cm^3) = 31.25 g = 25.20 cm^3

PBT = (42 cm^3 composites) × (40/100) × (1.30 g/cm^3) = 21.84 g = 16.80 cm^3

Total polymer = 31.25 + 21.84 = 53.09 g

Weight fraction of PLA = 31.25 / 53.09 = 0.589

Step 3 Calculation of amount of thermal stabilizer

Weight of thermal stabilizer = (Weight of composites) × (Weight fraction)

Irganox 1010 = (53.09 g) × (5000 × 10^{-6}) = 0.26 g

Irgafos 168 = (53.09 g) × (5000 × 10^{-6}) = 0.26 g

Step 4 Calculation of PLA and PBT content in the composites (95/5)

Volume of PLA = (Volume of composites) × (Volume fraction)

= (42 cm^3 composite) × (95/100)

= 39.9 cm^3 × (1.24 g/cm^3) = 49.48 g

Volume of PBT = (Volume of composites) × (Volume fraction)

= (42 cm^3 composite) × (5/100) = 2.1 cm^3

Step 5 Calculation of amount of composites (60/40) for dilution to composites (95/5)

Needed composites (60/40) = (Volume of PBT in composites (95/5)) ×

(Weight of composites (60/40) per volume of PBT)

= (2.1 cm^3) × (53.09 g / 16.80 cm^3)

= 6.63 g

Therefore,

PLA in needed composites (60/40) = (Weight fraction of PLA in composites) ×

(Weight of needed composites)

= (0.589) × (6.63 g) = 3.91 g

Thermal stabilizer in composites = (Weight fraction of thermal stabilizer) ×

(Weight of needed composites)

= $(5000 \times 10^{-6}) \times (6.63\ g) = 0.03\ g$

Step 6 Calculation of additional neat PLA and thermal stabilizer for kneading

Weight of additional PLA = Weight of PLA in composite (95/5) –

Weight of PLA in composite (60/40)

= 49.48 – 3.91

= 45.57 g

Weight of additional thermal stab. = Weight of thermal stab. in composite (95/5) –

Weight of thermal stab. in composite (60/40)

= 0.26 – 0.03

= 0.23 g

In summary, the contents of each material for preparation of all composites including spherical and fibrous dispersions are listed in Table A.1-A.3

Table A.1 Materials used for preparation of SP-S and FIBER-S

Materials	**Weight (g)**
Preparation of composites (90/10)	
PLA	46.88
PBT	5.46
Irganox 1010	0.26
Irgafos 168	0.26
Kneading into the composites (95/5)	
Composites (90/10)	26.17
Additional PLA	26.04
Additional Irganox 1010	0.13
Additional Irgafos 168	0.13

Table A.2 Materials used for preparation of SP-M and FIBER-M

Materials	**Weight (g)**
Preparation of composites (75/25)	
PLA	39.06
PBT	13.65
Irganox 1010	0.26
Irgafos 168	0.26
Kneading into the composites (95/5)	
Composites (75/25)	10.54
Additional PLA	41.67
Additional Irganox 1010	0.21
Additional Irgafos 168	0.21

Table A.3 Materials used for preparation of SP-L and FIBER-L

Materials	**Weight (g)**
Preparation of composites (60/40)	
PLA	31.25
PBT	21.84
Irganox 1010	0.26
Irgafos 168	0.26
Kneading into the composites (95/5)	
Composites (60/40)	6.63
Additional PLA	45.57
Additional Irganox 1010	0.23
Additional Irgafos 168	0.23

APPENDIX B

CALCULATION AND DATA OF VOID CONTENT

This is an example of calculation of void content of FIBER-L stretched by equibiaxial deformation at $\lambda_x \times \lambda_y = 3 \times 3$.

Importance information:

Bulk density before film stretching	1.2528	g/cm^3
Bulk density after film stretching	1.1611	g/cm^3

Assumption:

1. The film before stretching has zero void content
2. The film before stretching has weight of 1 g

The volume of film before stretching = 1 / 1.2528 = 0.7982 cm^3

The volume of film after stretching = 1/1.1611 = 0.8613 cm^3

Thus, the void volume of the stretched film = 0.8613 – 0.7982 cm^3 = 0.063 cm^3

And the void content of the stretched film = 0.063 / 0.8613 = 7.90 %

Table B.1 Bulk density and void content of SP-S samples

$\lambda_x \times \lambda_y$	No.	Bulk density (g/cm^3)	Void content (%)
	1	1.2476	-
	2	1.2560	-
1 × 1	3	1.2488	-
	Avg.	1.2508	-
	SD	0.0045	-
	1	1.2280	1.86
	2	1.2278	1.87
4 × 1	3	1.2328	1.46
	Avg.	1.2295	1.73
	SD	0.0028	0.23

Table B.2 Bulk density and void content of SP-M samples

$\lambda_x \times \lambda_y$	No.	Bulk density (g/cm^3)	Void content (%)
	1	1.2401	-
	2	1.2356	-
1 × 1	3	1.2671	-
	Avg.	1.2476	-
	SD	0.0170	-
	1	1.2255	1.80
	2	1.2188	2.36
4 × 1	3	1.2211	2.17
	Avg.	1.2228	2.11
	SD	0.0024	0.48

Table B.3 Bulk density and void content of SP-L samples

$\lambda_x \times \lambda_y$	No.	Bulk density (g/cm^3)	Void content (%)
	1	1.2451	-
	2	1.2397	-
1 × 1	3	1.2571	-
	Avg.	1.2473	-
	SD	0.0089	-
	1	1.2497	-0.19
	2	1.2512	-0.31
2 × 1	3	1.2515	0.11
	Avg.	1.2508	-0.13
	SD	0.0010	0.12
	1	1.2266	1.69
	2	1.2343	1.05
3 × 1	3	1.2280	1.97
	Avg.	1.2296	1.57
	SD	0.0041	0.47
	1	1.2189	2.33
	2	1.2337	1.10
4 × 1	3	1.2260	1.74
	Avg.	1.2262	1.72
	SD	0.0074	0.99
	1	1.2409	0.52
	2	1.2386	0.70
2 × 2	3	1.2353	0.97
	Avg.	1.2383	0.73
	SD	0.0028	0.23
	1	1.2177	2.43
	2	1.2065	3.38
3 × 3	3	1.2183	2.38
	Avg.	1.1242	2.73
	SD	0.0066	0.34

Table B.4 Bulk density and void content of FIBER-S samples

$\lambda_x \times \lambda_y$	No.	Bulk density (g/cm^3)	Void content (%)
	1	1.2597	-
	2	1.2476	-
1 × 1	3	1.2451	-
	Avg.	1.2508	-
	SD	0.0078	-
	1	1.2473	0.28
	2	1.2430	0.63
4 × 1	3	1.2450	0.47
	Avg.	1.2451	0.46
	SD	0.0022	0.18

Table B.5 Bulk density and void content of FIBER-M samples

$\lambda_x \times \lambda_y$	No.	Bulk density (g/cm^3)	Void content (%)
	1	1.2608	-
	2	1.2481	-
1 × 1	3	1.2492	-
	Avg.	1.2527	-
	SD	0.0070	-
	1	1.2165	2.98
	2	1.2208	2.61
4 × 1	3	1.2185	2.81
	Avg.	1.2186	2.80
	SD	0.0022	0.19

Table B.6 Bulk density and void content of FIBER-L samples

$\lambda_x \times \lambda_y$	No.	Bulk density (g/cm^3)	Void content (%)
	1	1.2409	-
	2	1.2609	-
1 × 1	3	1.2566	-
	Avg.	1.2528	-
	SD	0.0105	-
	1	1.2302	1.84
	2	1.2411	0.94
2 × 1	3	1.2328	1.62
	Avg.	1.2346	1.47
	SD	0.0057	0.47
	1	1.2183	2.83
	2	1.2245	2.31
3 × 1	3	1.2297	1.88
	Avg.	1.2242	2.34
	SD	0.0057	0.86
	1	1.1979	4.58
	2	1.1892	5.35
4 × 1	3	1.1937	4.95
	Avg.	1.1936	4.96
	SD	0.0057	0.54
	1	1.1971	4.65
	2	1.2076	3.74
2 × 2	3	1.2102	3.52
	Avg.	1.2050	3.97
	SD	0.0069	0.60
	1	1.1509	8.85
	2	1.1603	7.97
3 × 3	3	1.1721	6.89
	Avg.	1.1611	7.90
	SD	0.0106	0.62

APPENDIX C

LIST OF PUBLICATIONS

1. Samthong, C.; Deetuam, C.; Yamaguchi, M.; Praserthdam, P.; Somwangthanaroj, A. *The effects of size and shape of dispersed poly(butylene terephthalate) on isothermal crystallization kinetics and morphology of poly(lactic acid) composites* **J. Appl. Polym. Sci.** (Submitted).
2. Samthong, C.; Seemork, J.; Nobukawa, S.; Yamaguchi, M.; Praserthdam, P.; Somwangthanaroj, A. *Morphology, structure and properties of poly(lactic acid) microporous films containing poly(butylene terephthalate) fine fibers fabricated by biaxial stretching* **J. Appl. Polym. Sci.** 132 (2014): DOI: 10.1002/app.41415.
3. Samthong, C.; Somwangthanaroj, A.; Nobukawa, S.; Yamaguchi, M. *Structure and deformation behavior of poly(lactic acid)/poly(butylene terephthalate) blends*. **The 62nd SPSJ Symposium on Macromolecules**, September 11-13, 2013, Kanazawa, Japan (Poster Presentation).
4. Samthong, C.; Somwangthanaroj, A. *Melt functionalization of low density polyethylene with glycidyl methacrylate in the presence of comonomers and reactive blending with poly(lactic acid)*. **Frontier of Polymer in Science**, May 21-23, 2013, Sitges, Spain (Poster Presentation).
5. Samthong, C.; Somwangthanaroj, A. *Styrene and divinylbenzene-assisted melt grafting of glycidyl methacrylate onto low density polyethylene*. **Proceeding of Pure and Applied Chemistry International Conference (PACCON)**, January 23-25, 2013, Chon Buri, Thailand (Poster Presentation).

VITA

Mr. Chavakorn Samthong was born in Udon Thani on March 30, 1986. He received a bachelor's degree in engineering from Department of Chemical Engineering, Chulalongkorn University in 2008. He earned his master degree in engineering with emphasis in epoxy-based electronics packagings from Department of Chemical Engineering, Chulalongkorn University in 2010. During his master degree program, he went to do research involving epoxy composites filled functionalized silsesquioxanes with Prof. Richard M. Laine from Department of Materials Science and Engineering, University of Michigan (USA) for 7 months. After graduation, he joined the PhD program in engineering at Department of Chemical Engineering, Chulalongkorn University. Under the supervision of Assoc. Prof. Anongnat Somwangthanaroj, his work is focused on a development of microporous films from biodegradable poly(lactic acid) prepared by film stretching technique. Further, he also had collaboration with Prof. Masayuki Yamaguchi from School of Materials Science, Japan Advanced Institute of Science and Technology (Japan) for 8 months. After graduation, he would like to work in the company and get marry afterwards.